Stony Brook University

Mechanistic Studies in Heterogeneous Catalysis via *in situ* FT-IR Spectroscopy

A Dissertation Presented

by

Joseph W. Magee

to

The Graduate School

in Partial Fulfillment of the

Requirements

for the Degree of

Doctor of Philosophy

in

Chemistry

Stony Brook University

August 2016

Stony Brook University

The Graduate School

Joseph W. Magee

We, the dissertation committee for the above candidate for the
Doctor of Philosophy degree, hereby recommend
acceptance of this dissertation.

Michael G. White, Ph.D – Dissertation Advisor
Professor, Department of Chemistry

Peter Khalifah, Ph.D - Chairperson of Defense
Associate Professor, Department of Chemistry

Trevor Sears, Ph.D – 3rd Member of Defense
Professor, Department of Chemistry

Dario Stacchiola, Ph.D – Outside Member
Group Leader – Interface Science and Catalysis, Brookhaven National Laboratory

This dissertation is accepted by the Graduate School

Nancy Goroff

Interim Dean of the Graduate School

Abstract of the Dissertation

Mechanistic Studies in Heterogeneous Catalysis via *in situ* FT-IR Spectroscopy

by

Joseph W. Magee

Doctor of Philosophy

in

Chemistry

Stony Brook University

2016

Dependence on a finite supply of fossil fuel-based energy sources has provided motivation for research in and development of alternative, renewable energy sources. A strong candidate as an alternative fuel is ethanol. Ethanol has a high energy density, low toxicity, and as a liquid, compatibility with the existing fuel delivery infrastructure. When considering the possibility of using ethanol as a fuel, both synthetic methods to produce ethanol and reactions that convert ethanol to energy should be optimized. One method to produce ethanol is through the conversion of synthesis gas, or syngas, ($CO + H_2$). Currently, syngas conversion is used to produce methanol, diesel and gasoline. Recent discoveries in catalyst design have shown that a series of $RhFe/TiO_2$ and $RhFe/CeO_2$ catalysts promote the formation of ethanol under CO hydrogenation conditions [1, 2].

Once ethanol is produced it needs to be converted into energy in an efficient method. One approach for ethanol conversion is through ethanol electro-oxidation. In this reaction, ethanol is oxidized into several products (acetic acid, acetaldehyde, CO, CO_2), generating electrons. These

electrons can be collected to make electricity. Platinum electrocatalysts are highly active for C-C bond scission, but are quickly poisoned by CO that is formed during oxidation. Another complication arising for Pt systems is the formation of partial oxidation products, which limit the overall efficiency. The addition of SnO_2 nanoparticles to the Pt surface is known to improve current generation and the long-term stability of the Pt surface through a bifunctional mechanism in which SnO_2 activates H_2O to produce hydroxyls (-OH), which can be used to convert CO to CO_2 [3, 4].

This work focuses on the development of new experimental methods, techniques and instrumentation to investigate reaction pathways and reaction intermediates occurring on the surface of these working catalysts. Custom designed reactor cells that can be used to mimic reaction conditions are coupled with Fourier transform infrared (FT-IR) spectroscopy to study how the additions of Fe to Rh/TiO_2 and SnO_2 to polycrystalline (pc)-Pt affect selectivity and reactivity.

For SnO_2/pc-Pt, the deposition of SnO_2 nanoparticles directly onto the Pt surface via an ethylene glycol wet chemistry approach improves activity. The onset potential of EOR activity is negatively shifted by ~0.17V and there is 10-fold increase in current density, compared to pc-Pt alone. Infrared reflection absorption spectroscopy (IRRAS) measurements of the Pt surface under EOR conditions confirm the role of SnO_2 as an aid to $CO_{(ads)}$-Pt removal, which is evidenced by the complete removal of $CO_{(ads)}$ and the appearance of CO_2 at more negative potentials. IRRAS measurements also show the SnO_2/pc-Pt system promotes the formation of partial oxidation products, acetic acid and acetaldehyde.

In situ transmission FT-IR experiments on a series of $FeRh/TiO_2$ and $FeRh/CeO_2$ catalysts for CO hydrogenation provide improved understanding as to how these catalysts function under reaction conditions. CO adsorption on Rh/TiO_2 and Rh/CeO_2 shows that the CeO_2 support leads to an increased dispersion and smaller average particle size. The addition of Fe to these catalysts result in the appearance of a new CO band, likely due to CO adsorbed on Rh that is alloyed with Fe, confirming the presence of FeRh alloy at the surface of these catalysts. Comparing the transmission IR spectra under reaction conditions it becomes clear that Fe promotion improves ethanol selectivity by helping to deregulate CH_4 formation by breaking up large extended Rh^0 crystallites typically active for CO dissociation.

Contents

List of Tables

List of Figures

List of Abbreviations

CA: Chronoamperometry

CV: Cyclic voltammetry

DEFC: Direct ethanol fuel cell

EOR: Ethanol Oxidation Reaction

ECSA: Electrochemical Surface Area

FT-IR: Fourier Transform Infrared

HR-TEM: High Resolution Transmission Electron Microscopy

IRRAS: Infrared Reflection Absorption Spectroscopy

MCT: Mercury Cadmium Telluride

MIR: Mid Infrared

MOR: Methanol Oxidation Reaction

NPs: Nanoparticles

pc-Pt: polycrystalline Pt

PDF: Pair Distribution Function

STEM: Scanning Transmission Electron Microscopy

UHP: Ultra High Purity

UV: Ultraviolet

Vis: Visible

XRD: X-ray Diffraction

Dedication Page

This dissertation is dedicated to my parents and family.

Acknowledgments

First and foremost I'd like to acknowledge my parents. As cliché as it may sound, without them I wouldn't be here today writing these acknowledgements in my dissertation. They gave me support (in many ways) to get to this point and to get through the decades (maybe a slight exaggeration) of school that it took. I'd like to acknowledge my brother, because I know if I didn't mention him I'd never hear the end of it nor would I live it down.

I'd like to also acknowledge my adviser, Michael G. White, for his guidance during this whole wild ride that is graduate school. He gave me the freedom and guidance I needed to become a better scientist and also a few incredibly reasonable reminders of what it takes to earn a doctorate. During my time in graduate school I'd like to think I've matured and grown as both a person and scientist, and I owe an overwhelming majority of that to him.

Former group members that taught me what it meant to be a graduate student, and how to transition from an undergraduate know-a-lot to someone who realizes it's more fun when you get to learn something new than it is to think you know enough already. Drs. John Lofaro and Dan Wilson for being the first people I worked with and taught me all they knew about science, equipment, machining, design, etc. Dr. Robert Palomino for helping to realize that deep down inside I had a small XRD/EXAFS/PDF scientist that was going to come out, because I had no choice in the matter. Drs. Jing Zhou and Yixiong Yang for teaching me 0.0001% of the Mandarin language and making it clear that my Chinese foreign language skills are embarrassing at best.

Chapter 1. Introduction

The search for new renewable sources of energy, new methods to produce fuels and increased efficiency in energy generation will continue to be issues that require a multifaceted approach to be successful. Most traditional approaches include the use of a catalyst to help promote the formation of particular products, usually fuels (*e.g.* ethanol, methanol), or to help improve efficiency of energy generation. Moving forward, not only is it important to continue to develop new catalyst materials but also to continue to improve our understanding as to *why* a catalyst works and *how* it works under real conditions.

One experimental method that can be used to help better understand working catalytic systems is Fourier transform infrared (FT-IR) spectroscopy. FT-IR spectroscopy utilizes the interaction of IR radiation with individual molecular bonds, which all possess unique vibrational frequencies, to gain a handle on the types of molecular signatures that exist while a catalyst is working. The types of observables include both intermediates in a reaction pathway that are adsorbed on the surface of a catalyst and products that may have formed and remain either dissolved in solution or in the surrounding gas phase. In order to gain information about 'working' catalysts, it becomes necessary to make measurements *in situ* while exposing the catalyst surface to experimental conditions that mimic typical reaction conditions. Being able to replicate relevant reaction pressures and temperatures requires the design of functioning reactor cells that allow precise control over the local environment without negatively interfering with the incoming IR radiation. By coupling smart reactor cell design with smart catalyst design, it becomes possible to study reactions *in situ* in real time both for predominantly gas phase reactions (*i.e.* CO hydrogenation to ethanol) and in solution (*i.e.* ethanol electro-oxidation).

Efficient energy generation from the complete conversion of fuels to products is an important consideration in the design of catalysts. Direct ethanol fuel cells (DEFCs) represent a burgeoning technology that shows promise as a renewable source of energy [5-9]. In a DEFC, ethanol is oxidized at the anode to produce carbon dioxide. The corresponding cathodic reduction is the conversion of O_2 into H_2O. The electrons generated are collected and can be used to power devices along the external circuit between anode and cathode. The complete electro-oxidation of ethanol to CO_2 is a 12 e^- process, i.e., for every 1 ethanol molecule oxidized, potentially 12 e^- can be liberated. However, total oxidation is not the only reaction pathway. Many partial oxidation products such as acetaldehyde, acetic acid and carbon monoxide also form during the reaction. The potential reaction pathways for ethanol electro-oxidation are shown in Figure 1.1.

Pt-based electrocatalysts for the electro-oxidation of ethanol have been studied extensively [7-9]. Pt is a popular choice due to its ability to both adsorb and dissociate ethanol. Breaking the C-C bond to form $–CH_x$ and CO is a key step in full oxidation pathway to CO_2. In acidic solutions, CO is strongly bound to the Pt surface and is difficult to remove due to a lack of available oxidants (usually in the form of surface hydroxyls). This poisoning of Pt active sites limits the overall reaction efficiency and eventually deactivates the electrocatalysts. Only by applying a much higher potential is the $CO_{(ads)}$ removed from the Pt and activity returned.

In order to improve the efficiency of Pt-based EOR catalysts, deactivation of active Pt surfaces by $CO_{(ads)}$ must be minimized. One approach to limit surface poisoning is to add a metal oxide, such as SnO_2 to the Pt surface. The addition of SnO_2 is believed to improve overall activity by means of a bifunctional mechanism [10, 11]. That is, the presence of SnO_2 helps activate H_2O to form surface bound hydroxyls that can be used to further oxidize $CO_{(ads)}$ to CO_2.

Previous work on the SnO_2/Pt electrocatalyst system showed enhanced electrochemical activity for the methanol oxidation reaction (MOR) [12] and a strong size dependence [11]. By using only electrochemistry techniques, it is not possible to study the SnO_2-Pt interface or determine the concentration of CO on the Pt surface. By coupling electrochemistry and FT-IR spectroscopy it becomes possible to correlate differences in cyclic voltammetry, chronoamperometry and current generation with the state of the electrode surface using infrared reflection-absorption spectroscopy (IRRAS). By comparing the distribution of products and presence (or absence) of $CO_{(ads)}$ on SnO_2/Pt and Pt only, additional information as to the nature of the bifunctional mechanism and the SnO_2 promotional effect can be ascertained.

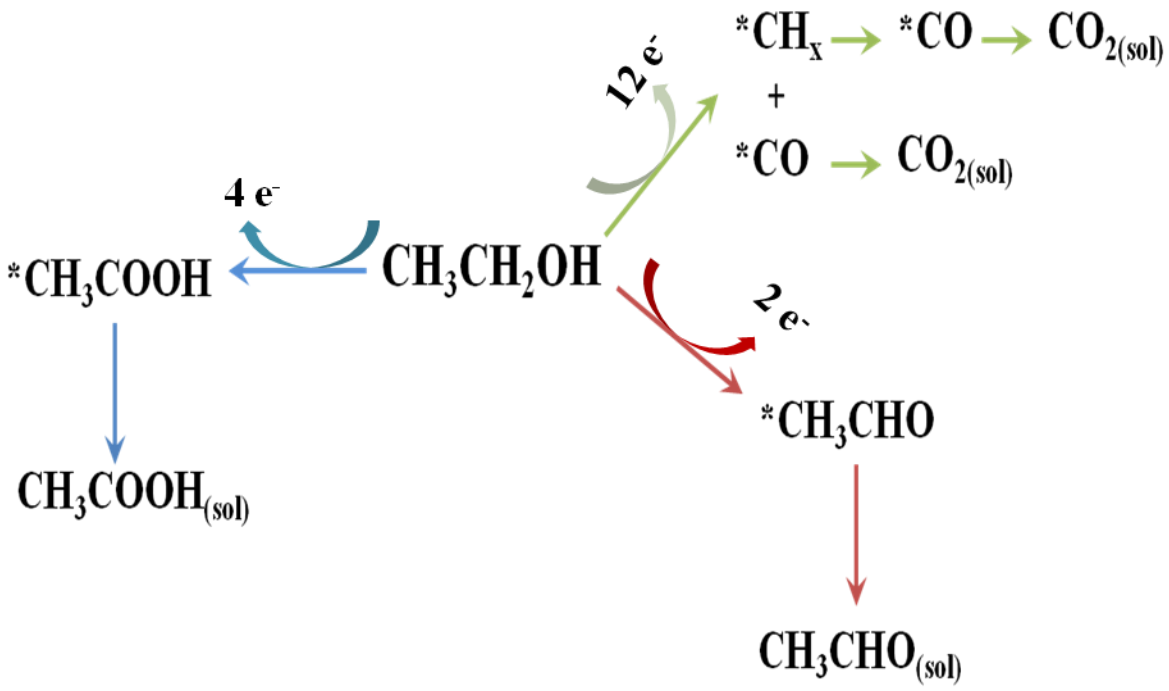

Figure 1.1: Representation of the ethanol electro-oxidation pathway on Pt electrodes. The red arrows show the 2 e^- pathway to produce acetaldehyde. The blue arrows show the 4 e^- partial oxidation pathway to acetic acid and the green arrows show the complete 12 e- pathway to produce CO_2. * represents a species bound to the Pt surface.

The conversion of synthesis gas, or syngas, (*e.g.* CO, H_2, CO_2) to value-added chemicals (*e.g.* methyl acetate, acetaldehyde) and liquid fuels (*e.g.* methanol and ethanol) is a promising reaction paradigm. To date, the most industrially successful catalyst in syngas conversion is Cu-ZnO/Al_2O_3, but only for the production of methanol [13]. Ethanol presents itself as a marked improvement, due to a higher energy density and non-toxicity. Thus far, no commercially viable ethanol synthesis catalysts have been developed. By analyzing the proposed reaction pathway for the conversion of CO and H_2 to ethanol, which is shown in Figure 1.2, it becomes clear that any potential catalyst needs to be able to (i) dissociate CO and H_2, (ii) regulate the hydrogenation of C_{ads} to CH_4, and (iii) promote C-C bond formation via CO insertion into a bound surface intermediate. Rh-based bimetallic catalysts supported on metal oxides have been shown to exhibit high ethanol selectivity at the expense of methane formation, compared to supported Rh alone. Transition metal promoters such as Fe, Mn, and Mo [14-16] have shown the highest enhancement in ethanol selectivity.

Previous reactivity measurements on $FeRh/TiO_2$ catalysts show an enhancement in ethanol selectivity as the Fe loading is increased up to ~3% wt loading [1]. This change in selectivity upon addition of a transition metal promoter is also reflected by a decrease in methane selectivity and an overall decrease in CO conversion. *In situ* X-ray diffraction (XRD) measurements after reduction show the formation of an FeRh alloy. The concentration of FeRh observed under reaction conditions correlates with ethanol selectivity. From this correlation it is posited that the active phase for ethanol formation is this alloy, and that the role of iron is likely to be as an active site blocker, or a simple deregulator of methane formation, which in turn allows more time for CO insertion on active surface-bound intermediates, leading to an enhancement in ethanol production.

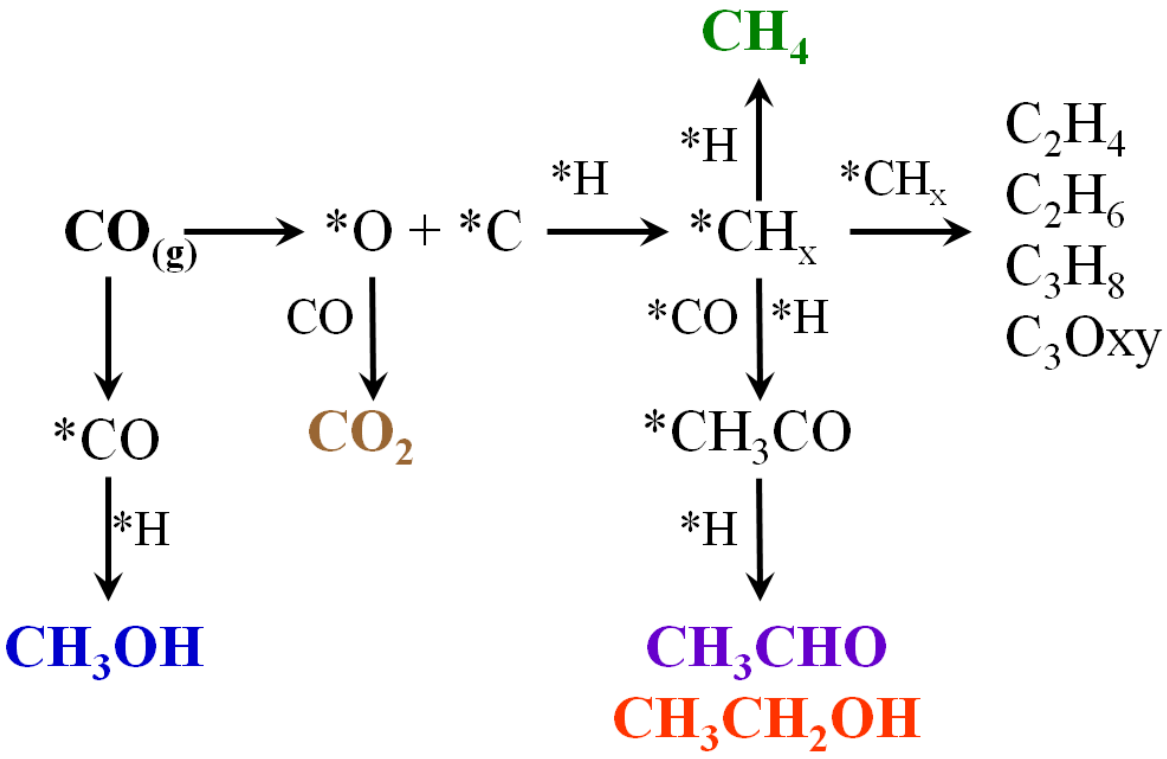

Figure 1.2: General reaction pathway for CO hydrogenation to ethanol. A species bound to the surface is represented by *.

These structural and reactivity measurements showed that Fe-addition to Rh-based catalysts altered the structure of the nanoparticle catalysts and changed the overall reactivity and selectivity. By further investigating these FeRh catalysts using FT-IR transmission spectroscopy, information about *only* the surface of the FeRh nanoparticles and any changes in the reaction pathway that Fe addition may promote can be determined. The adsorption of CO can be used to probe the surface composition of the catalysts. Spectra collected under reaction conditions (1:2 $CO:H_2$, 180-240 °C) help further clarify both the role of Fe in this system and how it alters the distribution of surface intermediates.

Chapter 2. Experimental Section

This Chapter describes in detail the experimental techniques used to acquire the data presented in this dissertation. Section 2.1 discusses the theory of Fourier Transform Infrared (FT-IR) spectroscopy in detail and how it is specifically applied to each of the catalyst systems studied. Section 2.2 describes the methods used to synthesize the catalysts and the experimental reaction cells used for *in situ* measurements. Section 2.3 outlines the electrochemical techniques used to characterize the SnO_2/Pt EOR catalysts discussed in Chapter 3.

2.1 Fourier Transform Infrared Spectroscopy

The most important experimental technique used in this dissertation is Fourier transform infrared spectroscopy. It is sensitive to many molecular vibrations present in the molecules and intermediates involved in the reactions studied here and allows for identification and assignment of these vibrational modes to specific bonds in a specific molecules.

Infrared spectra are the result of transitions between well defined, quantized vibrational energy states. Molecules with N number of atoms have 3N degrees of freedom. Six of these are due to rotational motion along x,y or z-axes and translational motion along the same. For non-linear molecules, that leaves 3N-6 degrees of freedom for vibrational modes. These modes involve a change in atomic position relative to their equilibrium position. The vibrational energy states (V_{iv}) of a harmonic oscillator can be described by equation (1)

$$V_{iv} = h\nu_i(v_i + \tfrac{1}{2}) \qquad (1)$$

where h is Planck's constant, ν_i is the frequency of the vibrational mode and v_i is the vibrational quantum number of the mode. However, this perfect harmonic oscillator is applicable only for

low values of v_i. At higher values of v_i, it becomes necessary to model the vibrational energy states (V_{iv}) as an anharmonic potential function. The anharmonic oscillator function is shown in equation (2).

$$V_{iv} = h\nu_i \left(v_i + \frac{1}{2}\right) + h\nu_i x_i (v_i + \frac{1}{2})^2 \quad (2)$$

where x_i is an anharmonicity constant. The main result of adding an anharmonicity component is to alter the selection rule such that changes in v_i greater than ±1 become allowed. In the mid infrared range, this consideration manifests as the appearance of weak overtone bands ($\Delta v_i > 1$) and combination bands ($\Delta v_i = 1$ and $\Delta v_j = 1$; where j is a different vibrational mode). For most vibrational modes, only a few atoms have large displacements from equilibrium while the rest of the molecule remains stationary. The frequency of this vibration is characteristic of the atoms only from which the motion is centered and can be used as a method to determine if a particular grouping of atoms is present.

A Bruker Vertex 80V spectrometer was used to collect all IR spectra presented. This spectrometer is designed around the concept of a Michelson interferometer. A Michelson interferometer is a device that divides a beam of radiation into two paths and then recombines the two beams after a path difference has been introduced between the two. It consists of two mirrors, one stationary and one that can be moved. The addition of a path difference creates a condition where interference between the two beams can occur. An example of a Michelson interferometer is shown in Figure 2.1.

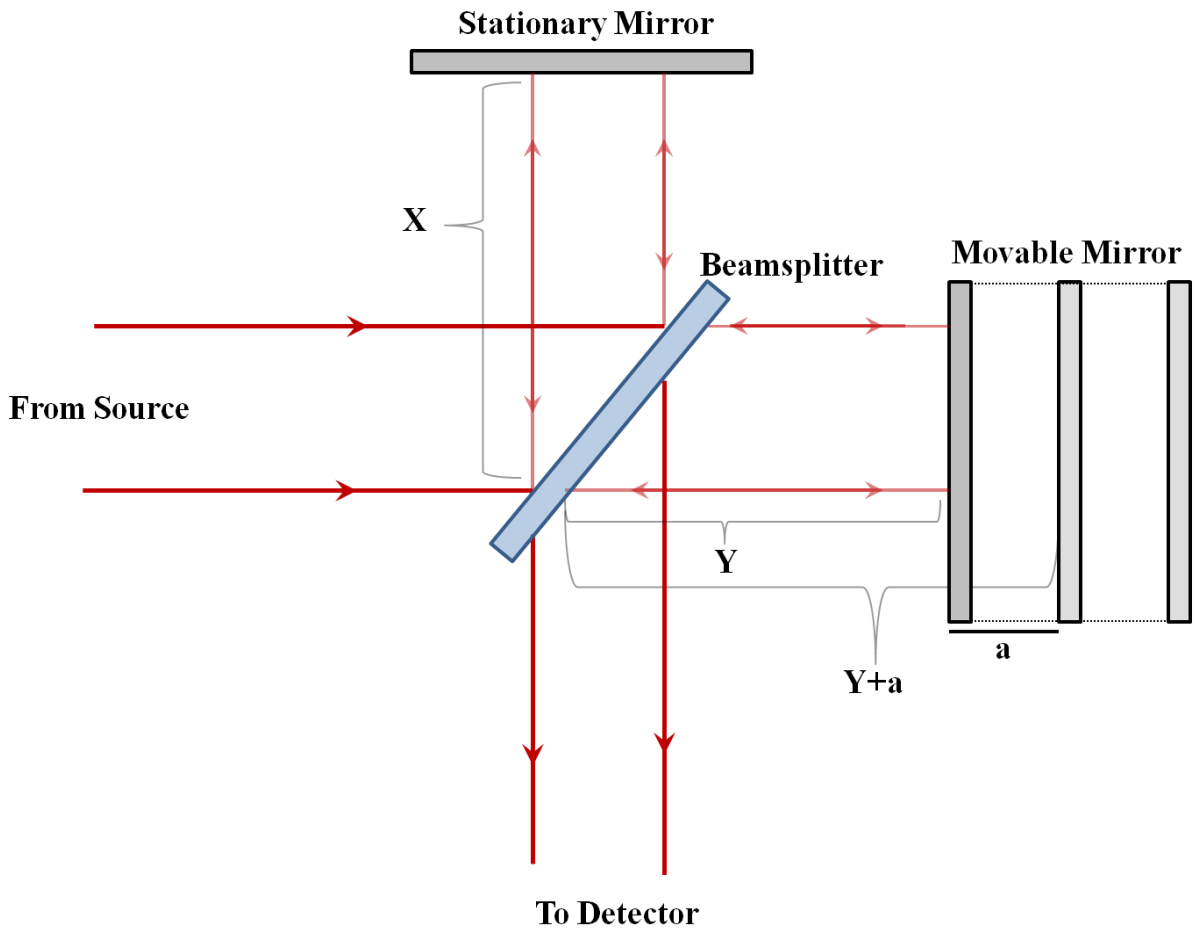

Figure 2.1: Diagram of a Michelson-type interferometer. The IR beam is split in two and directed onto a stationary mirror and a mirror moving at a constant velocity. The beams reflect off of the mirrors and recombine at the beamsplitter and are directed toward the detector. When the distance between the beamsplitter and stationary mirror (*X*) is equal to the distance between the beamsplitter and movable mirror (*Y*), the recombined beam interact constructively. When a path difference (*Y*+*a*) is added, the two beams interfere destructively. These repeated interactions generate an *interferogram.*

In between the two mirrors is a beamsplitter. As the IR beam passes through the beamsplitter, part is directed onto the moving mirror, while part is returned to the fixed mirror. The recombined beam is the directed through the sample compartment and then to the detector. The interference signal measured by the detector is called an interferogram. Every data point of the interferogram contains information about every frequency emitted by the source. In order to transform the interferogram into a MIR frequency spectrum, a mathematical operation known as a Fourier transform is used. A Fourier Transform F(v) of a time domain signal f(t) is determined by Equation (3).

$$F(v) = \frac{1}{\sqrt{2\pi}} \int_{-\infty}^{\infty} f(t) \cos(2\pi v t)\, dt \qquad (3)$$

Once the Fourier transform is applied to the data contained within the interferogram, a spectrum with an x-axis of frequency in cm^{-1} results.

2.1.1 Data Acquisition and Handling

All data acquisition is handled using the OPUS suite of spectroscopy software provided by Bruker. The FT-IR spectrometer is fully computer controlled. For most experiments, unless otherwise noted, A SiC globar MIR source is used. The beam is shrunk down by passing through a 4 mm aperture. Saturation of the detector occurs at >32,000 counts, so the beam size is adjusted to prevent saturation via this aperture. The beam then passes through a KBr beam splitter and is directed into the sample compartment by a series of focusing mirrors. The sample compartment is isolated from the optical bench by 2 KBr windows, mounted on either side of the sample compartment. The windows allow for venting of the sample compartment to exchange samples while keeping the optical bench of the spectrometer under vacuum (~3 Torr). After passing

through the sample compartment, the beam is focused to the detector. For all the experiments in this dissertation, a mid-band LN_2-cooled MCT detector (Infrared Associates) is used. A layout of the beam path is shown in Fig 2.2. Sample spectra in the range of 4000-800 cm^{-1} are averaged over 128 totals scans at a resolution of 4 cm^{-1} and a scanner velocity of 40 kHz. All resultant spectra are presented in absorbance mode and are referenced to a relevant background scan. After collection, spectra are manipulated with a combination of smoothing (5 or 9 pt depending on S/N), background corrections (rubber band correction or manually), peak integration and spectrum subtraction.

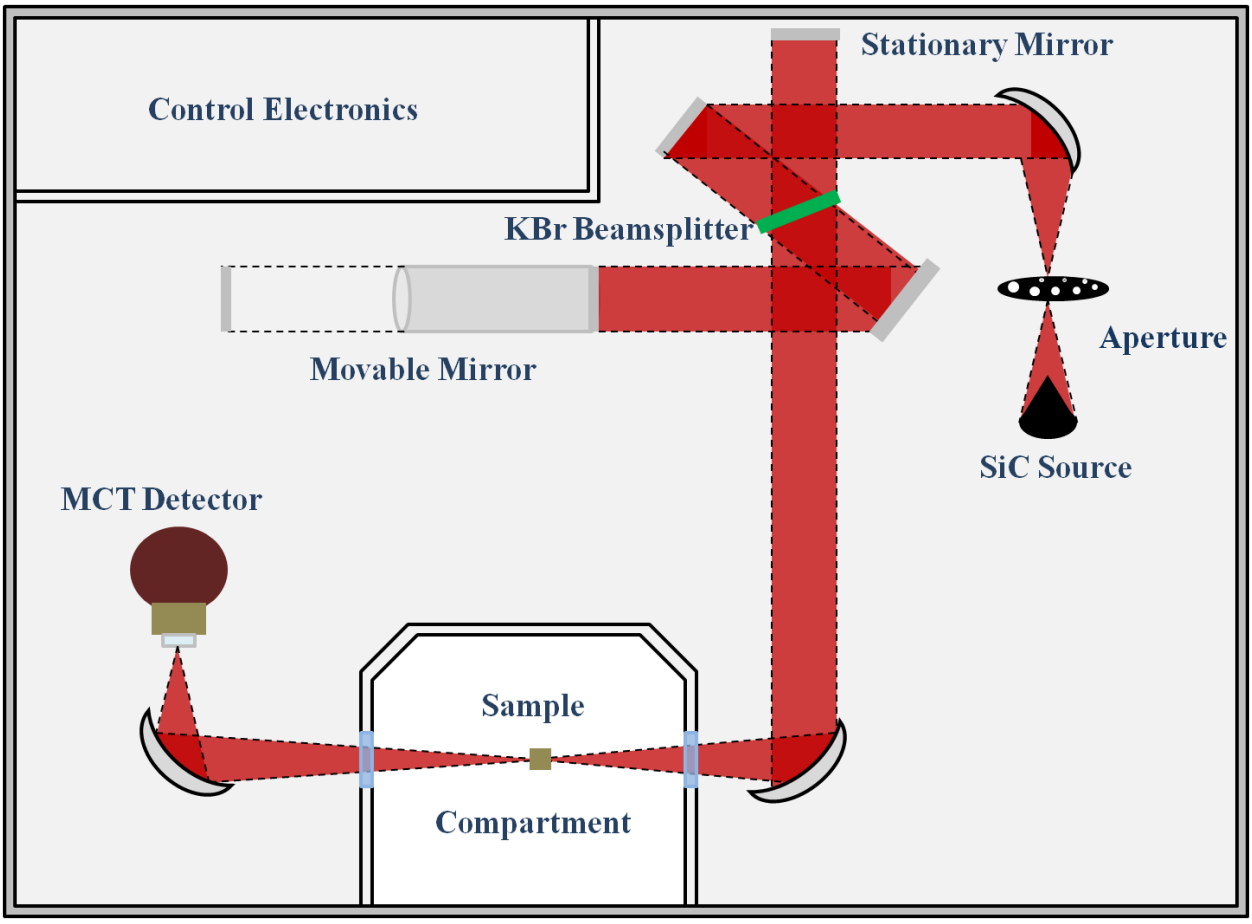

Figure 2.2: Beam path of the Bruker Vertex 80V Spectrometer. The MIR radiation generated by the SiC source is focused onto two mirrors; one stationary, one moving. After recombining the beam is focused into the sample compartment and then re-focused onto the window of the MCT detector.

2.2 Experimental setup for *in situ* experiments

The diversity of experimental systems studied in this dissertation required the design, construction and implementation of unique systems. For electrochemistry, the reactor cell itself needs to be inert and designed in such a way to be able to focus the IR beam onto the surface of a *working* pc-Pt electrode while immersed in solution. To study CO hydrogenation on FeRh-based catalysts, a reactor is needed that allows: (i) heating of the sample (for reduction and reaction) (ii) integration with a gas handling manifold for reactant gases (iii) being able to reach pressures in the range of 5×10^{-8} Torr and (iv) maintaining the vacuum within the spectrometer. In order to perform photochemical experiments, all of the considerations for CO hydrogenation still need to be met, while managing to get UV light onto the surface of the material.

2.2.1 SnO_2/Pt ethanol electro-oxidation

In order to investigate the EOR pathway on a pc-Pt electrode with and without the addition of SnO_2 nanoparticles, a custom designed reaction cell was developed. A schematic representation of this cell is shown in Figure 2.3. The design of this cell is based on an IRRAS geometry, wherein the pc-Pt crystal, in addition to being a working electrode, also functions as an IR radiation mirror. Using this geometry, the IR beam passes through the reaction solution twice, sampling any aqueous phase products that may have formed (e.g. acetic acid, CO_2, acetaldehyde) as well as any products still bound to the catalyst surface (e.g. CO). The Teflon reactor cell is mounted in a VeeMax II (Pike Technologies) accessory, which consists of a series of mirrors that direct the incoming IR beam to the pc-Pt surface. A CaF_2 window at the base of the reactor cell allows IR transmission below 1000 cm^{-1}. The reference electrode is Ag/AgCl and

a Pt wire serves as the counter electrode. A wire is spot-welded to the backside of the pc-Pt working electrode and all three electrodes are connected to a potentiostat (Autolab). For EOR spectroelectrochemical measurements, all three electrodes are immersed in a solution containing 0.5 M ethanol in 0.1 M $HClO_4$.

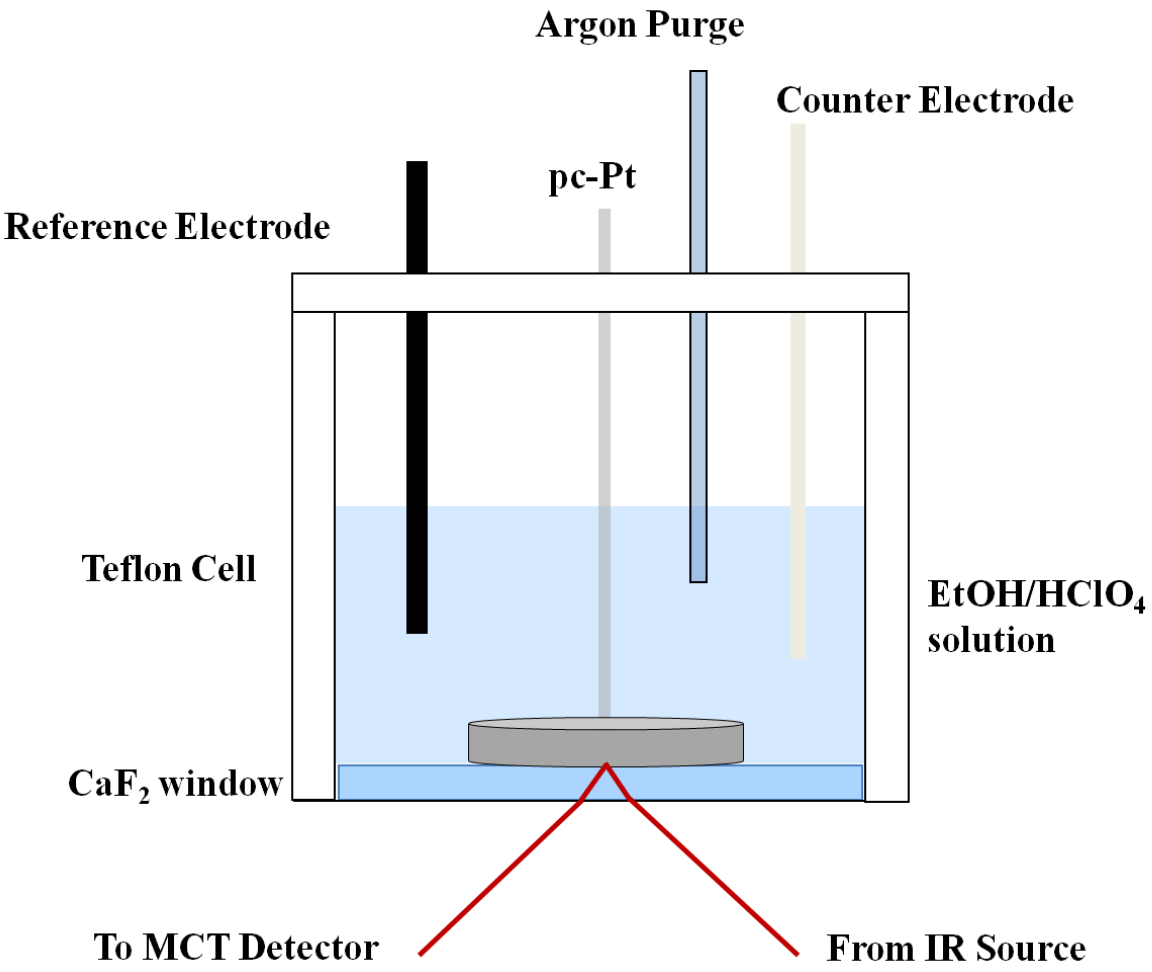

Figure 2.3: A schematic representation of the electrochemical setup used for all SnO_2/pc-Pt experiments.

2.2.2 FeRh/TiO_2 CO hydrogenation

Compared to crystalline surfaces, powder catalysts require a different experimental setup. Due to their lack of reflectivity, IRRAS cannot be used. Fortunately, TiO_2 and CeO_2 supported catalysts can be studied using transmission FT-IR spectroscopy by placing the sample directly in the path of the incoming beam. The experimental setup for the transmission experiments is shown in Figure 2.5. A hydraulic press is used to embed a tungsten mesh (0.2 mm aperture, 64% open area, Goodfellow) with (Fe)Rh/TiO_2 catalyst. This catalyst loaded mesh is then clamped onto a Ni sample holder which is connected to a vacuum feed through to allow the sample to be resistively heated to >400°C or cooled using liquid N_2 to ~ -173°C. A type-K thermocouple is spot welded directly to a bare spot on the mesh to measure the sample temperature under reaction conditions. An example of a mounted sample is shown in Figure 2.4.

The sample is mounted to an xyz manipulator that can be used to position the sample in the IR beam. Being able to move the sample in-and-out of the beam path allows for multiple samples to be measured at once as well as being able to center the sample in the IR path. In the case of CO adsorption on FeRh/TiO_2 and FeRh/CeO_2 samples containing similar iron loadings were studied in pairs (1FeRh/TiO_2 and 1FeRh/CeO_2) to minimize the chance that slightly different pretreatment conditions could lead to any observed differences in CO adsorption behavior. For CO hydrogenation experiments, only a single sample was loaded at a time so that any observation of gas phase product formation (e.g. CH_4) could be attributable only to the catalyst sample in the beam path.

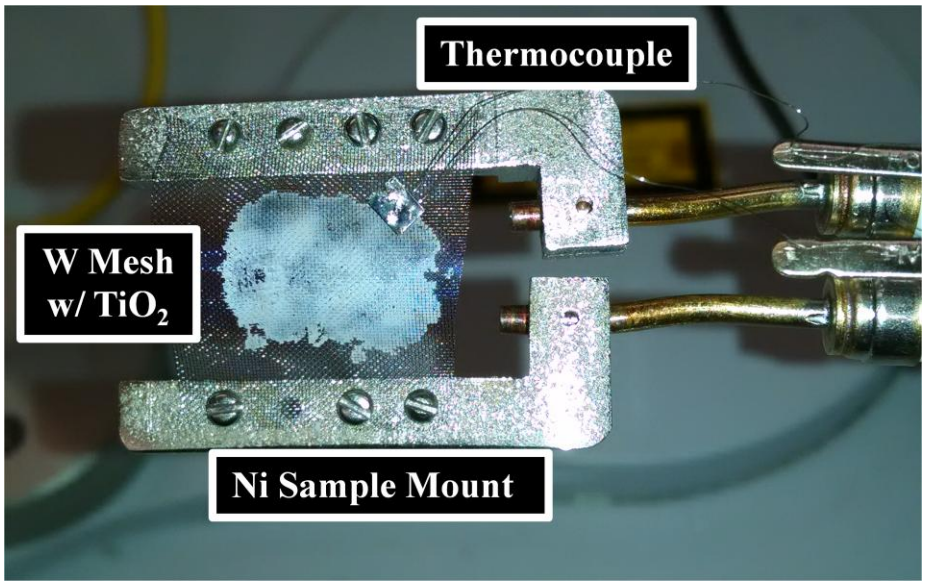

Figure 2.4: Experimental view of a TiO_2 sample mounted in the Ni sample holder. The TiO2 sample is pressed into the tungsten mesh using 20,000 psi from a hydraulic press. After mounting the mesh, a thermocouple is spotwelded to the mesh to measure the reaction temperature.

A custom designed reactor cell was designed and used in order to expose the supported FeRh catalyst to reactant molecules in a controlled fashion. The cell is designed based on a 6-way stainless steel UHV cross. The two ports parallel to the IR beam are sealed with ZnSe windows (MPF Products, Inc.). ZnSe is transparent in the mid-IR range and does not strongly react with either CO or H_2. The in-plane ports perpendicular to the IR beam are used for gas handling. Two stainless steel tubes are welded to the rear flange for gas dosing and evacuation with a turbomolecular pump. The front flange contains an exhaust tube for gases for experiments where flow of gases is required. This design isolates the reactor cell from the spectrometer while maintaining the vacuum seal of the spectrometer, removing the need for dry air or nitrogen purging of beam path to remove any CO_2 or $H_2O_{(g)}$ in the air. This allows the cell to be evacuated to pressures as low as 10^{-8} Torr and sample exchange without having to vent the spectrometer. Gas handing is controlled via a manifold made up of 4 mass flow controllers (MKS) independently connected to a flow controller. The gases typically used in these experiments are H_2 (for reduction and hydrogenation), CO (for adsorption at active sites and reaction) O_2 (for oxidation and cleaning) and N_2/He (for purging). The flow rate is set by the controller and then fed directly into the reactor cell. For experiments that require adding a known quantity of gas, the pressure in the reactor cell can be measured by a thermocouple gauge (Granville Phillips) connected to the reactor cell.

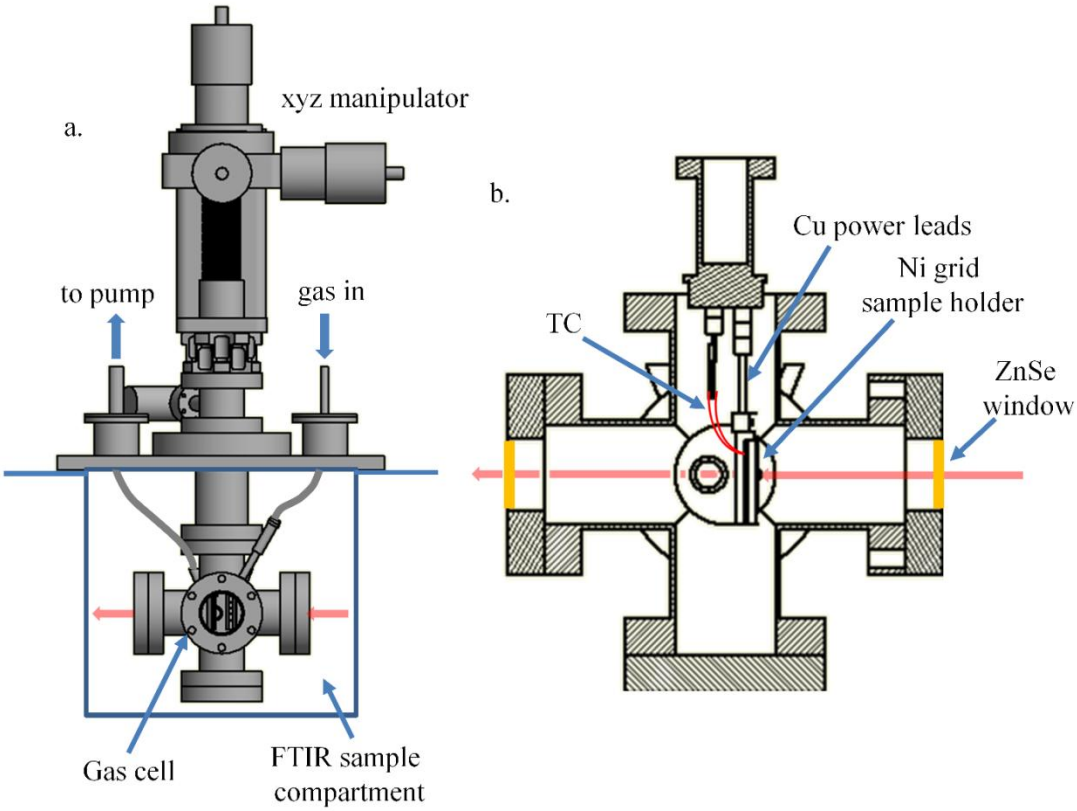

Figure 2.5: Representation of the vacuum FT-IR cell used in these experiments (a) Front view of xyz-stage mounted to sample plate and mounted in sample compartment of spectrometer. (b). Cross-sectional view of the IR cell perpendicular to IR beam when used in CO hydrogenation experiments.

2.2.3 TiO_2 photochemistry

Photochemistry experiments utilize the same reactor cell discussed in section 2.1.2 with a few slight modifications. The front sample compartment plate has been modified to accommodate the admission of light into the reactor cell. A fiber optic coupler and collimator (Accuglass Inc.) have been attached to the front plate. The coupler is sealed such that it, too, does not interfere with the sample compartment vacuum. A UV transparent window has also been attached to the reactor cell to allow UV/Vis light to reach the mounted TiO_2 sample. The coupler is attached to LED diodes (Prismatix) outputting either 365nm (UV) or 515nm (Vis). The sample is no longer positioned perpendicular to the IR beam. In order to be able to make sure the IR beam is passing through a section of the catalyst that is also being irradiated, the sample is rotated ~45° towards the incoming UV light. The UV light feedthrough design can be seen in Figure 2.6

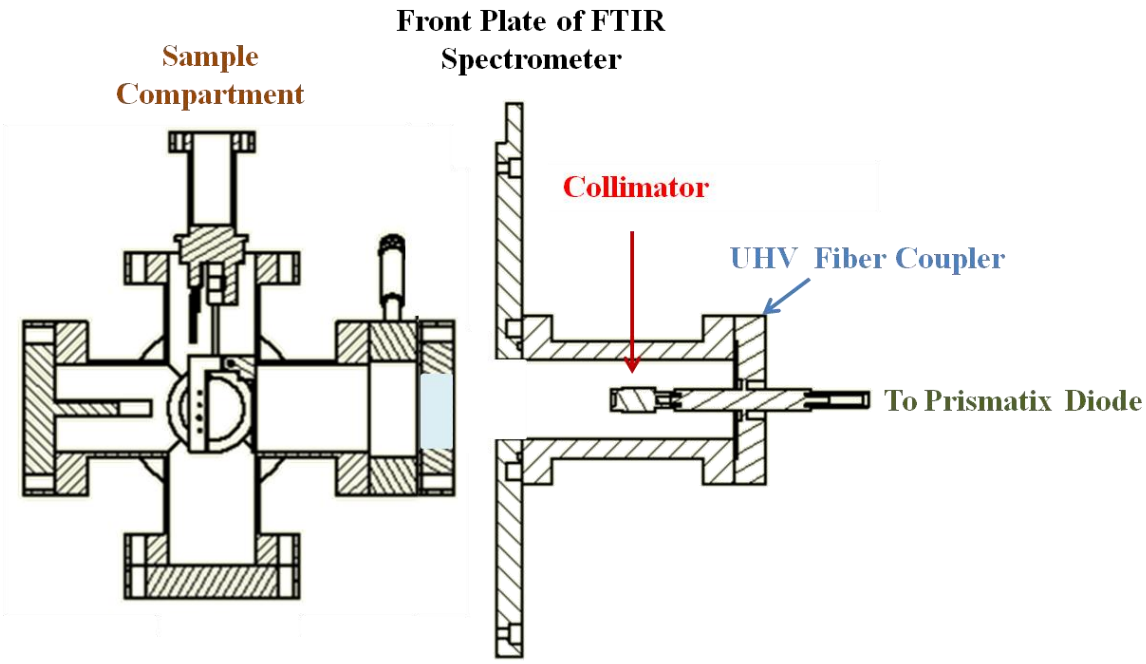

Figure 2.6: Experimental setup for photochemistry experiments. The view shown is looking down the axis of the IR beam. A UHV fiber coupler and mount is connected directly to the sample compartment plate of the spectrometer and is sealed with an o-ring. A UV transparent window on the front port of the transmission cell allows light to reach the sample. Note the 45° change in orientation compared to Figure 2.5.

2.3 Catalyst synthesis

All catalyst syntheses presented in this dissertation were carried out either at the Center for Functional Nanomaterials (CFN) or in the labs of the Surface Electrochemistry and Electrocatalysis group at the Chemistry Department at Brookhaven National Laboratory.

2.3.1 SnO_2 nanoparticles on pc-Pt

SnO_2 nanoparticles are synthesized using the ethylene glycol (EG) method. All glassware was steam cleaned and baked prior to use. For the synthesis, a 3-necked round bottom flask is connected to a jacketed condenser. 6 mL of ethylene glycol is added to the flask with a stir bar. The flask is then added to an oil bath set to a temperature of 200°C with a stir rate of 800 RPM. While the ethylene glycol is heating, 58mg of $SnCl_2 \cdot 2H_2O$ (Sigma Aldrich) is dissolved in 4 mL of ethylene glycol and sonicated. When the temperature of the heated ethylene glycol reached 190 °C, the $SnCl_2$ solution was injected into the hot solution. In order to begin the "reaction clock", 150 μL of MilliQ UHP H_2O was injected into the reactant solution. The size of the SnO_2 particles formed depends on the elapsed time from injection of H_2O to when the solution is removed from the round bottom flask, transferred to a clean vial and chilled in the freezer for 1-2 minutes. The cooled solution is then sonicated for 15 minutes to improve the dispersion of the nanoparticles.

In order to prepare the SnO_2/pc-Pt electrocatalyst, a pc-Pt crystal is cleaned via electrochemical cycling. A known quantity, typically ~20 μL of the SnO_2 colloid suspension is deposited on the pc-Pt surface and allowed to dry in air. After deposition, the electrode was

cleaned in 0.1 NaOH to remove any residual ethylene glycol or Cl^-. More details about the experimental synthesis procedure can be found in Chapter 3 of this dissertation.

2.3.2 Rh and FeRh nanoparticles supported on TiO_2 and CeO_2

The powder catalysts studied in Chapter 4 of this dissertation were prepared via wet impregnation of nanoparticulate metal oxide powders, TiO_2 (P-25 Degussa-Evonik) and CeO_2 (Sigma Aldrich). Rhodium (III) nitrate hydrate ($Rh(NO_3)_3 \cdot H_2O$) and iron (III) nitrate nonahydrate ($Fe(NO_3)_3 \cdot 9\ H_2O$) were used as Rh and Fe sources, respectively. Solutions of the metal precursors are added drop-wise to the metal oxide powder until a paste is formed. The weight percent of Rh is held constant at ~2% for all catalysts while the iron loading is varied from 0 to 8% to produce a range of $FeRh/TiO_2$ or CeO_2 catalysts. The loaded paste is then dried overnight in an oven at 120 °C before calcination in air at 450 °C for 4 hours. After this step, the catalyst is ground into a fine powder with a mortar and pestle. The reactivity of these catalysts toward CO hydrogenation to ethanol are studied in depth in Chapter 4 of this dissertation.

2.3.3. Photodeposition of Metal Particles onto TiO_2

Another method for creating metal oxide supported catalysts is using photo-deposition. Photo-deposition takes advantage of the electrons generated during band gap excitation of the semiconductor (i.e. TiO_2) to reduce metal cations in solution and form nanoparticles on the TiO_2 surface. During band-gap excitation, photogenerated holes and electrons migrate to the TiO_2 surface. When a metal ion, M^+, is in close proximity to the electron at the TiO_2 surface, it can be reduced to M^0, which results in the formation of a metal nanoparticle. A diagram of the

experimental photo-deposition reactor can be seen in Figure 2.7. A known amount of metal precursor salt (*e.g.* $RhCl_3 \cdot xH_2O$, H_2PtCl_6, $FeCl_3$, AgCl, AuCl) is dissolved in DI water to create a solution with a known amount of the metal. This solution is added to a quartz vial containing ~100 mg P-25 TiO_2. A small amount of methanol is added as a hole scavenger. The reaction vial is sealed and purged with dry N_2 for 30 min in the dark with stirring. The cell is then irradiated by a Xe arc lamp (Oriel) for a fixed duration of time; the longer the irradiation time, the larger the particles formed. After irradiation, the metal-loaded TiO_2 is collected via either filtration or evaporation of the remaining solution.

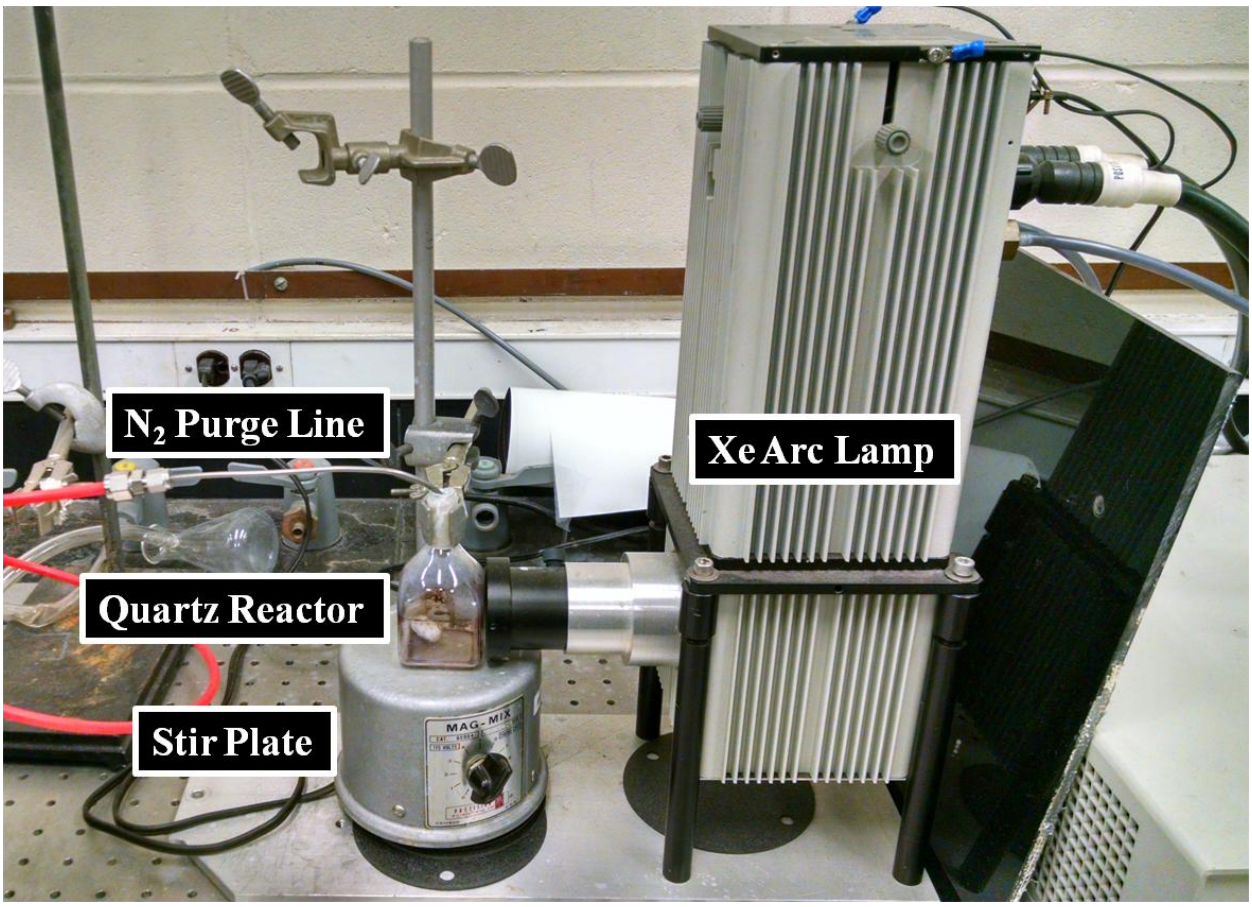

Figure 2.7: Photodeposition experimental setup. The quartz reactor is sealed with parafilm prior to ignition of the Xe arc lamp. TiO_2 + M^+ solution omitted for clarity.

2.4 Electrochemical Techniques

2.4.1 Cyclic Voltammetry (CV)

Cyclic voltammetry is an electrochemical technique that measures the current that is created in an electrochemical cell by sweeping the potential applied to a working electrode linearly over time in a cycle. The potential is applied between the working electrode (pc-Pt in these experiments) and the reference electrode (Ag/AgCl) while the current is measured between the working electrode and counter electrode (Pt wire). In general, it is used to study the electrochemical properties of an analyte in solution. A representative CV plot of potential vs. current is shown in Figure 2.8. Anodic (positive) current is observed during oxidation of the analyte while cathodic (negative) current is seen during a reduction process. Faradaic current is the rise in measurable current and is attributed to an oxidation/reduction reaction of the analyte in solution. Capacitive current is a result of charge cycling within the double layer of ions adsorbed on the electrode surface. It can be considered similar to a background current within the electrochemical cell itself.

CV based techniques can also be used to measure the active surface area of an electrode. During pc-Pt reduction, protons from solution become adsorbed at the electrode surface. During oxidation, H atoms desorb as H^+ and an electron. By measuring the current generated during desorption, removing the contribution of the double layer and accounting for the geometric area of the electrode, it becomes possible to calculate the electrochemical surface area (ECSA) of the working electrode. For Pt, this value is ~210 $C \cdot cm^{-2}$. Experimentally determined values not in line with this number are usually the result of contaminants, a rough electrode surface, or blocking of Pt sites by other metals or metal oxides (i.e. SnO_2).

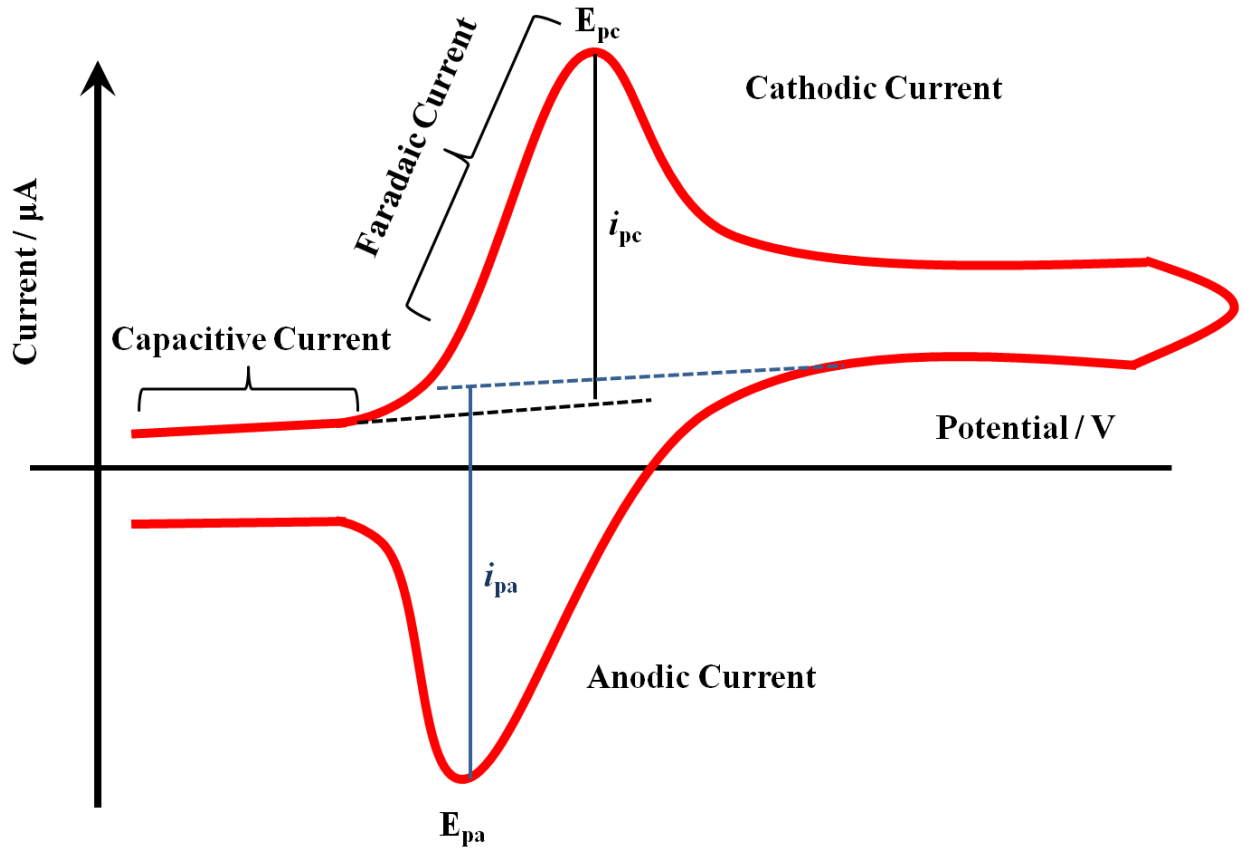

Figure 2.8: Representative reversible cyclic voltammogram. E_{pc} and i_{pc} represent the cathodic peak potential and peak current, respectively while E_{pa} and i_{pa} represent the corresponding anodic peak potential and peak current.

2.4.2 Chronoamperometry (CA)

A second electrochemical technique used in this dissertation is chronoamperometry. In CA, a working electrode is immersed in a solution containing the analyte of interest. A constant potential, typically at a voltage where an oxidation/reduction process occurs, is applied to the electrode. The current is measured as a function of time. By measuring the current over time, qualitative information about the stability of the working electrode can be gained and a comparison between activity of a reference (pc-Pt) and experimental (SnO_2/pc-Pt) system can be made.

Chapter 3. Promotion of Pt Surface for Ethanol Electro-Oxidation by the Addition of SnO_2 Nanoparticles: Activity and Mechanism.

This section was published in *Applied Catalysis B- Environmental*, 2014,152, 397-402

3.1. Introduction

Ethanol is attractive for fuel cell applications considering its availability from renewable sources, high energy density and low environmental impact as compared with other liquid fuels such as methanol and formic acid.[17] However, the slow kinetics and inefficient conversion of ethanol to CO_2 at low temperatures and low potentials hinder its wide-spread application. The complete oxidation of an ethanol molecule to CO_2 involves many elementary reaction steps, including C-C bond splitting, water activation to form -OH, and the oxidation of CO and CH_x intermediates into CO_2.[18-20] Although Pt surfaces with low coordination sites are able to split the C-C bond,[5, 8, 18-24] Pt alone is not an efficient catalyst for the ethanol oxidation reaction (EOR). This is due to the formation of strongly bound CO and CH_x intermediates, which poison Pt surfaces at low potentials.[8, 18, 23, 24] Extensive efforts have been undertaken to identify and understand co-catalyst materials that can alleviate CO poisoning of Pt catalysts and improve the overall reaction kinetics.

Platinum-based catalysts promoted by the addition of tin oxides have been reported to have higher reactivity for the EOR compared to Pt itself.[3, 4, 10, 25-27] Previous studies on mixed Pt/tin oxide powder samples using *in situ* infrared spectroscopy and differential electrochemical mass spectroscopy (DEMS) were able to detect reaction intermediates and products such as CO,

CO_2, acetaldehyde and acetic acid.[3, 4, 10, 27] However, the complexity of these Pt/SnO_2 binary nanocatalysts has led to some controversy regarding the nature of the active phase and the origin of their high EOR activity. For example, the enhanced EOR activity has been generally assigned to a bi-functional mechanism wherein the SnO_2 promotes water dissociation at low potentials, which enhances the oxidative removal of chemisorbed CO_{ads} at nearby Pt sites.[3, 4, 10, 27] Measurements used to test this hypothesis are complicated by the presence of a Pt-Sn metallic alloy phase, often found in Pt/SnO_2 powders, which influences EOR activity and selectivity in a way that is different from Pt/SnO_2 interface sites.[6, 7, 27-30] In addition, the strong dependence of catalytic performance of Pt/SnO_2 powder catalysts on synthetic methods and activation conditions further impedes a clear understanding of the catalytic effect of SnO_2 co-catalysts in ethanol oxidation.

Recent studies in our laboratory demonstrated that the deposition of SnO_2 nanoparticles (NPs) on planar Pt surfaces can be used as models of complex Pt/SnO_2 binary powder catalysts to investigate the chemical properties of SnO_2 and Pt/SnO_2 interface sites for electro-oxidation of methanol and ethanol.[11, 12] Specifically, our studies showed that small SnO_2 NPs (~2 nm) deposited on a polycrystalline Pt (pc-Pt) electrode strongly enhance catalytic performance for methanol oxidation, while larger NPs (~20 nm) show a negligibly small promoting effect.[12] Prior to electrochemical measurements, X-ray photoelectron spectroscopy (XPS) measurements show that both small and large SnO_2 NPs are dominated by Sn(IV) species. Interestingly, post-electrochemical reaction studies detected reduced Sn(II) species on SnO_2/Pt surfaces with ~ 2nm SnO_2 NPs, but not with 20 nm NPs.[12] The enhanced activity was attributed to the presence of reduced Sn(II) species in small SnO_2 NPs.[12]

In the present work, we use a model SnO_2/pc-Pt catalyst to investigate the catalytic effect of SnO_2 in the EOR. Catalytic activity, reaction mechanism and surface morphology are studied by a combination of electrochemical methods and *in situ* infrared reflection-absorption spectroscopy (IRRAS). The electrochemical measurements clearly demonstrate that the deposition of small (~2 nm) SnO_2 NPs on a pc-Pt electrode significantly enhances the EOR reactivity of Pt. The *in situ* IRRAS study provides mechanistic information on the catalytic role of SnO_2 NPs, as well as a comparison of the product distribution and selectivity of bare pc-Pt and SnO_2/pc-Pt surfaces. The insights gained from these results are expected to have important implications for further development of SnO_2/Pt based electrocatalysts for ethanol electooxidation.

3.2. Experimental

3.2.1 Preparation of SnO_2 (NPs)/pc-Pt electrode

0.25 mmol $SnCl_2 \bullet 2H_2O$ (99.99%, Sigma Aldrich) was dissolved in 4 mL ethylene glycol (Sigma Aldrich, 99.8%). This solution was then injected into a three-neck round bottom flask with 6 ml ethylene glycol that was pre-heated to 190°C. High-purity water (Nanopure, Thermo Scientific) was added to the mixture to give a ratio of water to ethylene glycol of ~0.02. The solution was then refluxed at 190°C and vigorously stirred in air for 40min to obtain tin oxide NPs.[25] The tin oxide colloid was immediately quenched in an ice-water bath after reaction. Figure 3.1a and 3.1b show the HRTEM image of the SnO_2 NPs and the corresponding size distribution, respectively, indicating an average particle size of ~2.5 nm.

The freshly-prepared tin oxide NPs dispersed in ethylene glycol were sonicated for ca. 15 min before being deposited on a cylindrical polycrystalline Pt electrode. In a typical procedure, the electrochemical surface area (ECSA) and roughness factor of the Pt electrode was first determined in 0.1 M $HClO_4$ solution. Then, a certain volume of the tin oxide solution (20 μl for the present work) was pippetted onto the pc-Pt electrode surface. After precipitation in air for several hours, the tin oxide covered Pt electrode was dipped into 1.0 M NaOH and then ultra-pure water to remove residues such as ethylene glycol and Cl^- ions. The as-prepared electrode was then cycled in a blank solution followed by ethanol activity measurements in a different cell. In order to prevent SnO_2 dissolution and maintain its promotional effect, the potential is not cycled beyond 0.5V.Right after the activity testing, the Pt electrode, partially covered with ~ 2 nm tin oxide NPs, was transferred into a three-electrode Teflon cell for IRRAS measurements.

3.2.2 Electrochemical Measurements

All electrochemical experiments were performed at room temperature in a 0.1 M $HClO_4$ solution made with UHP H_2O and using an Autolab 128N potentiostat. An Ag/AgCl (sat. Cl^-) electrode (Bio) was used as the reference electrode. Currents in the present work are normalized to the bare Pt surface area using the H_{upd} charge after double layer correction assuming a value of 210 $\mu C/cm^2_{Pt}$. Prior to each electrochemical measurement, the solution was purged with argon gas for at least 30 minutes to remove dissolved oxygen.

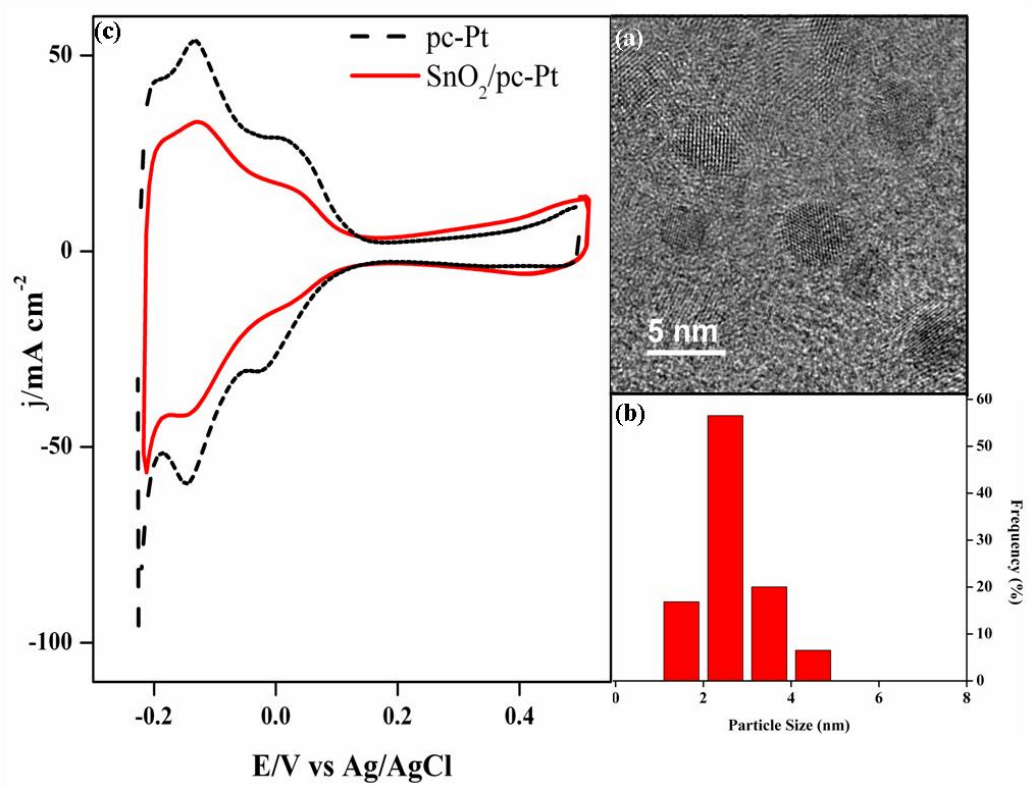

Figure 3.1: (a) TEM image of SnO_2 deposited onto a pc-Pt electrode; (b) corresponding particle size distribution; (c) comparison of voltammetric curves for 2 nm SnO_2 NPs supported on pc-Pt- and bare pc-Pt in 0.1 M $HClO_4$ solution. Scan rate: 50 mV s^{-1}. Currents in the present work are normalized to the bare Pt surface area (H_{upd} charge after double layer correction), prior to SnO_2 deposition, assuming a relationship of 210 $\mu C/cm^2_{pt}$.

3.2.3 IRRAS measurements

IR spectra were acquired using a Bruker Vertex 80V spectrometer equipped with a mid-band MCT detector at a spectral resolution of 4 cm^{-1}. The IRRAS cell utilizes a commercially available Teflon spectroelectrochemical cell (VeeMaxII, Pike Technologies) modified to accommodate 3 electrodes and an Ar purge line. A CaF_2 window was used to allow for IR transmission. Transmission was still >20% at 900cm^{-1}. The polycrystalline Pt working electrode was pressed against the window to create a thin solution layer with a thickness of a few micrometers. A Pt foil and a leak-free Ag/AgCl electrode were used as the counter and reference electrode, respectively. The sample compartment was purged with Ar prior to IR measurements in order to remove spectral interference from CO_2 and water vapor in air. Initially the potential was held at -0.2 V vs. Ag/AgCl for 195 s, while a background scan was collected and used as the reference for all sample spectra. The potential was then stepped in the positive direction in 50 mV increments. A total of 128 single channel spectra were collected and averaged. Three scans were collected at each potential, 3 minutes apart, yielding a total time held at each potential of ~ 450sec. Spectra are given in absorbance units defined as $A = -\log(R/R_0)$, where R and R_0 represent the reflected IR intensities corresponding to the sample and reference-single beam spectrum, respectively.

3.3 Results and Discussion

Figure 3.1c compares the cyclic voltammagrams (CV) of a pc-Pt electrode partially covered with SnO_2 NPs with a bare pc-Pt electrode in 0.1 M $HClO_4$ solution. Deposition of SnO_2 NPs on the Pt electrode decreases the available Pt surface sites and a ~45% loss of Pt surface area from the change in H-desorption charge is estimated. The SnO_2/pc-Pt electrode shows stable CV features with continuous cycling up to 0.5 V.

Figure 3.2a compares polarization curves for ethanol oxidation over the SnO_2/pc-Pt electrode and the bare pc-Pt electrode in a 0.5 M ethanol in 0.1 M $HClO_4$ solution at room temperature. Deposition of SnO_2 NPs on the pc-Pt electrode results in an active surface for the EOR that exhibits a large negative shift in the onset potential (~0.17 V) and a significantly higher current compared to the bare pc-Pt electrode. Chronoamperometric measurements shown in Figure 3.2b confirm the enhancement in catalytic performance and stability for the SnO_2/pc-Pt electrode. After running the reaction for 1600 s at a potential of 0.20 V at room temperature, the SnO_2/pc-Pt electrode still exhibited high activity, with a measured current density of ~ 65 $\mu A/cm^2$. This is more than a 10–fold increase in current density compared with the bare pc-Pt electrode (5 $\mu A/cm^2$).

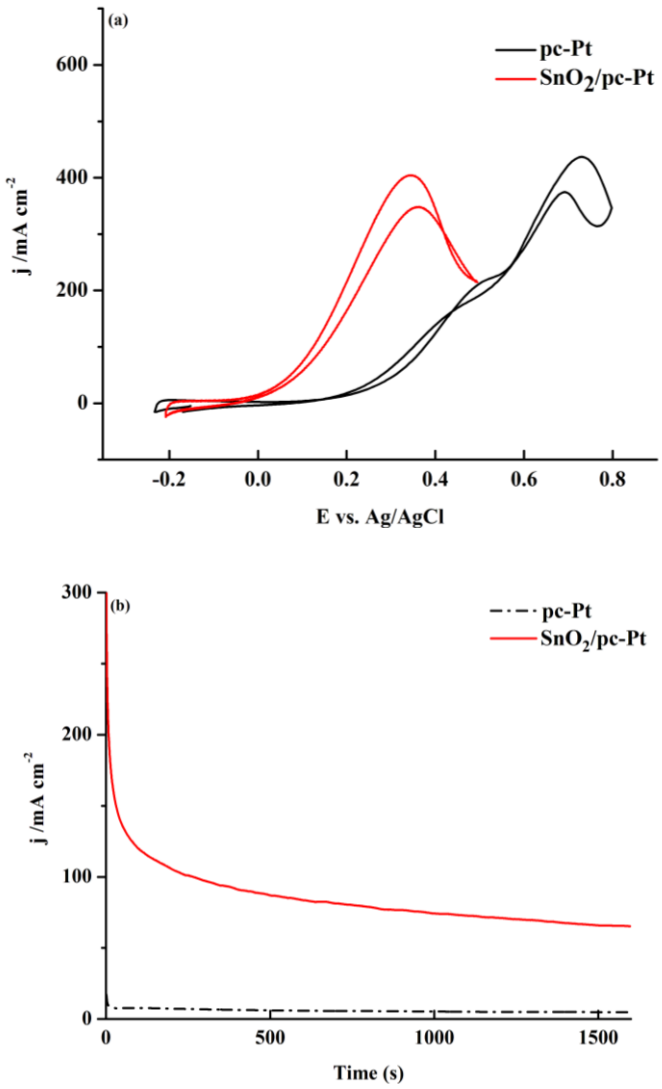

Figure 3.2: (a) Comparison of current-potential polarization curves for a pc-Pt electrode decorated with SnO_2 NPs (red line) and a bare Pt electrode (black line) in 0.5 M ethanol and 0.1 M $HClO_4$ solution. Sweep rate is 10 mV/s. (b) Comparison of current-time plots for ethanol oxidation activity on the pc-Pt electrode with SnO_2 NP's (red) and a bare pc-Pt electrode (black) in a ethanol solution at 0.20 V for 1600 s reaction time at room temperature.

In situ IRRAS measurements were carried out to investigate the surface intermediates and product distribution for the potentiodynamic oxidation of ethanol on the SnO_2/pc-Pt and bare Pt electrodes. Figures 3.3 show IRRAS spectra at applied potentials in a 0.5 M ethanol in 0.1 M $HClO_4$ solution in the range of 2500-2000 cm^{-1} for both bare (a) pc-Pt and (b) SnO_2/pc-Pt. The band centered around 2050 cm^{-1} can be assigned to linear bound CO_{ads} on Pt, indicating that C-C bond cleavage of adsorbed ethanol has occurred. As the potential is swept towards more positive potentials a peak appears near 2343 cm^{-1}, which can be assigned to the asymmetric stretching vibration of CO_2 in solution; this CO_2 is the product of the complete oxidation of ethanol. Similarly, the wavenumber region 1350-850 cm^{-1} is shown in Figure 3.4. The bands at 1280 cm^{-1} and 933 cm^{-1} are characteristic features of acetic acid and acetaldehyde, the main partial oxidation products, in solution. The spectral region 1150-1025 cm^{-1} contains two peaks. The peak that increases with potential at 1110 cm^{-1} is attributed to the adsorption of ClO_4^- while the peak at 1045cm^{-1} is assigned to the C-O stretch of ethanol. A list of the experimentally observed frequencies and their assignments is given in Table 3.1.

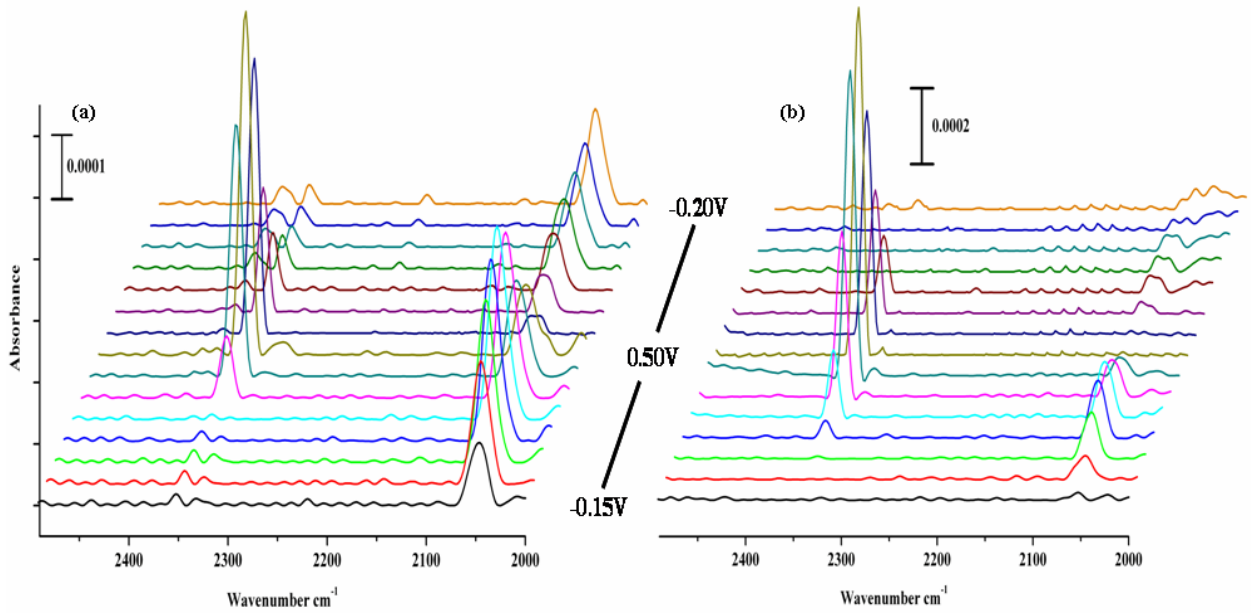

Figure 3.3: *In situ* IRRAS spectra in the range 2500-1900cm^{-1} recorded during ethanol electro-oxidation in 0.5 M ethanol in 0.1 M $HClO_4$ solution: (a) a bare Pt electrode; (b) a SnO_2/pc-Pt electrode. Reference spectrum was taken at a potential of -0.20 V.

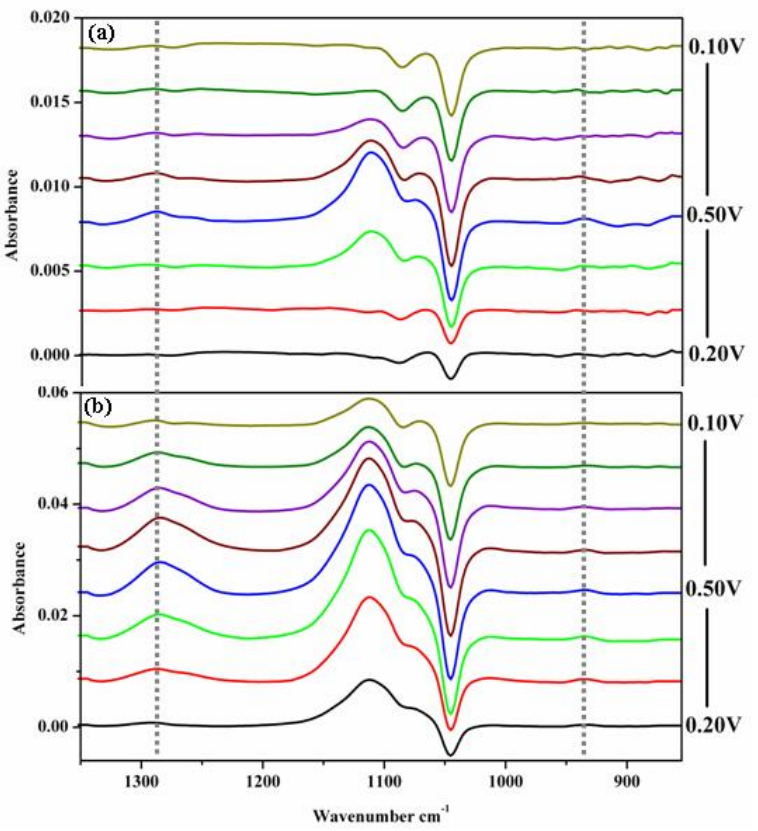

Figure 3.4: *In situ* IRRAS spectra in the range 1350-950cm^{-1} recorded during ethanol electro-oxidation in 0.5 M ethanol in 0.1 M $HClO_4$ solution: (a) bare Pt electrode; (b) SnO_2/pc-Pt electrode. Reference spectrum was taken at a potential of -0.20 V.

Although carbon monoxide, carbon dioxide and acetic acid are the main species observed on both SnO_2/pc-Pt and pc-Pt electrodes, their changes in intensity with potential are different. Figure 3.5a shows a comparison of integrated intensities for the vibrational bands for CO_2 (~ 2343 cm^{-1}) and CO (~ 2050 cm^{-1}) plotted as a function of electrode potential. Similar data for acetic acid (~ 1280 cm^{-1}) and acetaldehyde (933cm^{-1}) are shown in Figure 3.5b. For the pc-Pt electrode, the band intensity of CO_{ads} is negligible at -0.2 V and increases with potential to a maximum at 0.25-0.3 V, and then drops down to almost zero at 0.55 V. This dependence of the CO_{ads} vibrational band on applied potential is in good agreement with previous studies of the ethanol oxidation on pc-Pt electrodes by FT-IR,[23, 24] SFG, [18] and ATR-SEIRAS.[8] The observation of the CO_{ads} band clearly indicates that there are Pt active sites on the pc-Pt electrode capable of breaking the ethanol C-C bond.

Although the general trends of the intensity profiles for the CO_{ads} and CO_2 bands are similar for the SnO_2/pc-Pt and bare pc-Pt electrodes, there are two distinct differences. First, its noted that the CO_{ads} band intensity begins to decrease at 0.15 V on SnO_2/pc-Pt, which is ~ 0.15 V lower than that on the bare Pt electrode and coincident with the appearance of the CO_2 band (Figure 3.5a). This negative potential shift in the maximum CO_{ads} band intensity is a clear indication of the catalytic effect of the SnO_2 NPs for the EOR on Pt. The promoting effect of small SnO_2 NPs is associated with oxidative removal of CO_{ads} on Pt sites, and is consistent with our previous study of the MOR on a SnO_2/pc-Pt electrode.[12] Secondly, note from Figure 3.5a that the overall band intensity of CO_{ads} on the SnO_2/pc-Pt surface is about ~ 45% lower than that on the bare pc-Pt electrode, which is quite close to the loss of Pt surface area obtained from cyclic voltammetry (Figure 3.1). Hence, the reduction of Pt surface sites on the SnO_2/pc-Pt electrode appears to have a negligible effect on CO_2 formation.

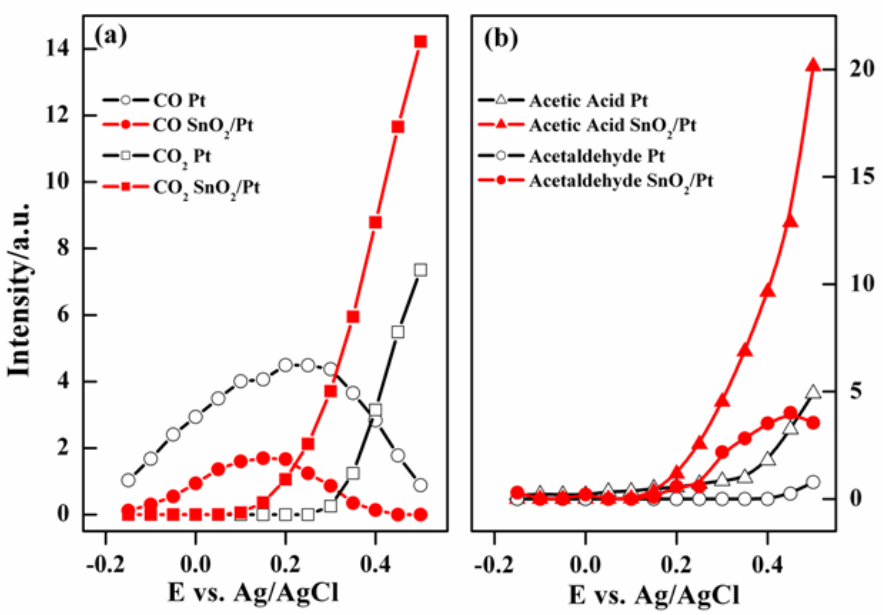

Figure 3.5: Integrated band absorption as a function of applied potential for both the bare pc-Pt and SnO_2/Pt electrodes: (a) CO_2 and linear-bound CO_{ads}; (b) acetic acid and acetaldehyde.

The larger CO_2 integrated band intensity for the SnO_2/pc-Pt surface suggests that CO_2 formation is enhanced even though the available Pt surface has been reduced by SnO_2 particle deposition.

Addition of SnO_2 NPs on the Pt surface not only facilitates the complete oxidation of ethanol to CO_2, but also increases the production of acetaldehyde and acetic acid as evidenced by the IR bands at 933 cm^{-1} and 1280 cm^{-1}, respectively. Figure 3.5b shows that the integrated band intensities for acetic acid and acetaldehyde are considerably larger on the SnO_2/pc-Pt electrode than the bare pc-Pt electrode. Noticeably, the onset potential (~ 0.15 V) of acetic acid formation occurs coincidently with the decrease of the CO_{ads} band and the appearance of the CO_2 product band. These observations suggest that SnO_2 NPs enhance both complete (CO_2) and incomplete (acetaldehyde/acetic acid) oxidation pathways for EOR on Pt. Since C-C bond breaking is expected to occur on Pt sites, the decrease in Pt surface area (~ 45%) on the SnO_2/pc-Pt electrode may result in a relatively larger accumulation of C_2 intermediates which then undergo facile oxidation at SnO_2/Pt interfaces.

In a second *in situ* IRRAS measurement, a constant potential of 0.2 V was applied and IRRAS spectra were followed with reaction time in an attempt to better understand the chronoamperometric measurements (Figure 3.2). Static thin-layer studies are subject to mass transport limitations, which may promote the re-adsorption of intermediates and further oxidation, and the appearance of pH and diffusion gradients over time, which may alter product distribution.[31] However, identical experimental conditions should still allow for a meaningful comparison to be made between pc-Pt and SnO_2/pc-Pt product distribution over time. The integrated band intensities corresponding to the formation of CO_{ads}, CO_2 and acetic acid with reaction time are presented in Figure 3.6. A negligible change with polarization time for the CO, CO_2 and acetic acid bands was observed on the pc-Pt electrode at 0.2 V. Since the highest

coverage of CO_{ads} is also near 0.2 V (see Figure 3.5a), the pc-Pt surface is therefore completely blocked for further ethanol adsorption and oxidation, consistent with the negligible current observed in the CA measurement (Figure 3.2b). By contrast, the CO_2 and acetic acid band intensities with polarization time on the SnO_2/pc-Pt electrode show completely different behavior. Most importantly, the CO_2 band intensity steadily increases with polarization time but the CO_{ads} band intensity remains constant (Figure 3.5a). This is a clear indication that complete oxidation of ethanol to CO_2 occurs at 0.2 V on the SnO_2/pc-Pt electrode. However, partial oxidation of ethanol is also occurring at this potential as evident from the even larger increase in band intensity for acetic acid.

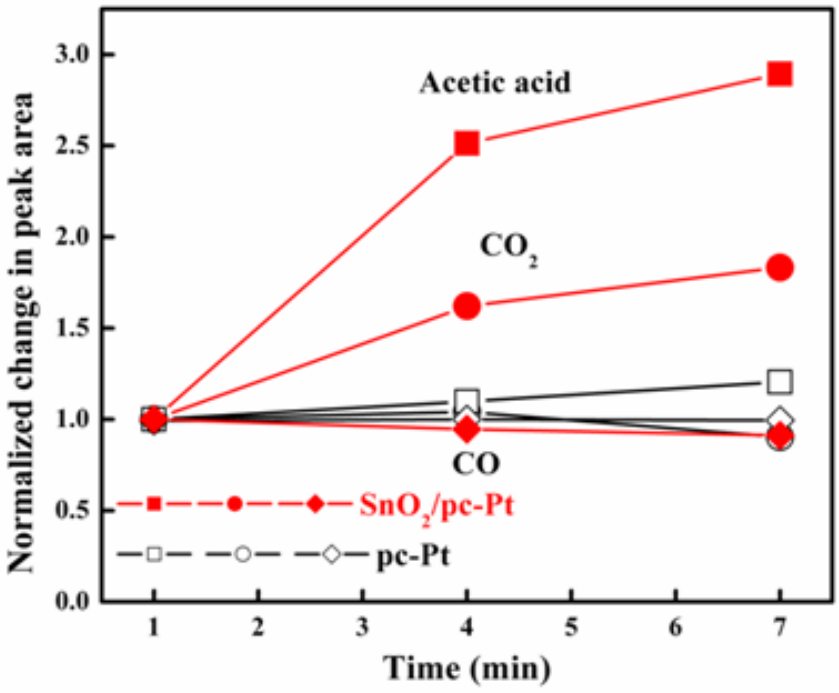

Figure 3.6: Normalized band intensities of linear-bound CO_{ads}, CO_2, and acetic acid (1280 cm^{-1}) under a constant polarization of 0.2V over time. The band intensities for all three species at a given reaction time were normalized to the one recorded after 1 min of polarization. This normalization provides a better visual description of product evolution with reaction time.

Numerous studies have shown that C-C bond splitting can occur on Pt surfaces at low applied potentials.[8, 9, 18-24, 32] Density functional theory (DFT) calculations also suggest that there are no large barriers in the pathways leading to CO_{ads} and acetic acid formation.[5] However, further oxidation of CO_{ads} and $CH_{x,ads}$ is hindered at potentials relevant to fuel cells, where water dissociation on Pt is difficult.[8, 18, 24] Therefore, the chemisorbed CO and CH_x intermediates accumulate on the surface and block the Pt surface sites for ethanol adsorption and oxidation, as confirmed by our IRRAS measurement. Adding SnO_2 NPs as a co-catalyst on the pc-Pt surface leads to significantly enhanced activity and is assigned to the facile oxidation of CO_{ads} at low potentials (Fig. 3.4 and 3.5), which is related to the relative ease of water dissociation on SnO_2 NPs to form oxidizing -OH species. However, introducing -OH species to the Pt surface also increases the partial oxidation products (acetic acid and acetaldehyde), which leads to higher current densities, but lower selectivity and efficiency to CO_2.

Recently, Kavanagh et al., reported DFT calculation results for ethanol oxidation on a bare Pt surface with and without the presence of OH species [5]. They suggested that the formation of OH species on the Pt surface leads to a considerably increased reaction barrier for C-C bond splitting and hence inhibits CO_{ads} formation and CO_2 production. For the SnO_2/pc-Pt binary system, less available Pt sites for ethanol adsorption and reaction leads to a reduced formation of CO_{ads} (Figure 3.3b). Interestingly, an increase, rather than a decrease in the CO_2 formation is observed in the entire potential region, including at potentials where the CO_{ads} can be oxidized at the bare Pt surface. Therefore, it's believed that the Pt active sites on the SnO_2/pc-Pt electrode are not affected by the OH species at nearby SnO_2 sites and retain their ability to catalyze the full oxidation of ethanol. The data presented here, however, do not specifically address the effects of

SnO_2 NPs on the oxidation of adsorbed CH_x intermediates, which could be an important issue for the complete oxidation of ethanol on SnO_2/Pt(111) surfaces.[9, 33]

Given that acetic acid formation also involves surface OH species via the reaction CH_3CO + OH → CH_3COOH,[5] it is likely that the availability of OH species at SnO_2-Pt interface sites also decreases the reaction barrier and thereby increases its production rate. Since ethanol oxidation has been shown to have a strong dependence on the Pt surface structure,[5, 8, 18-24] a controlled deposition of a SnO_2 co-catalyst that avoids covering Pt sites active for C-C bond splitting is likely to improve ethanol conversion to CO_2. In this regard, Del Colle et al.[9] demonstrated that the electrochemical deposition of Sn on Pt step sites on a Pt(332) surface increases acetic acid formation due to a decrease in the available Pt active sites for C-C bond splitting. It is expected that the polycrystalline Pt surface used in this work to have a large number of steps and other defect sites (e.g., grain boundaries) which could act as active sites for C-C bond splitting such as those found for highly stepped surfaces. In this work, however, SnO_2 nanoparticles are randomly deposited on the pc-Pt surface and not selectively at steps as in the work of Del Colle et al.[9]. Hence, some defect sites will clearly be blocked, which will decrease the effectiveness of C-C bond splitting, but deposition will also occur on the terraces, presumably where acetic acid and acetaldehyde are preferentially formed. Despite having fewer active sites exposed on the SnO_2 covered pc-Pt surface, the results in Figures 3.5a and 3.5b show that the yields of both the total (CO_2) partial oxidation (acetaldehyde and acetic acid) products are enhanced. Further improving the catalytic selectivity of SnO_2/Pt catalysts may be achieved by optimizing the SnO_2/Pt surface, for example, by strategically depositing SnO_2 at Pt terrace sites to block the acetic acid formation pathway while keeping the low-coordination Pt sites for C-C bond splitting. Alternatively, the catalytic efficiency of SnO_2/Pt may be improved by adding

a third element to the catalyst surface, such as Rh, that is more effective for C-C bond splitting.[3, 4] Ongoing studies in this area involve investigating the mechanism of EOR on well-defined, UHV prepared SnO_2/Pt electrocatalysts, including the addition of a second metal to enhance C-C bond splitting and selectivity.

3.4 Summary

The present study of a pc-Pt-supported SnO_2 NPs system clearly demonstrates the catalytic effect of SnO_2 nanoparticles in promoting the electrooxidation of ethanol and provides new insight into the reaction mechanism on SnO_2/Pt binary catalyst surfaces. The enhanced electrochemical activity of SnO_2/pc-Pt electrodes for the EOR is evidenced by a negatively shifted onset potential of ~ 0.17 V and a 10-fold increase in current density at low potentials (0.2 V). Our study suggests that the enhanced activity is directly linked to the catalytic function of SnO_2 co-catalysts, which provides OH species for the effective oxidative removal of surface CO_{ads}. Moreover, *in situ* IRRAS results also suggest that the presence of OH species provided by the SnO_2 NPs does not affect the C-C bond splitting ability of Pt active sites, which is also a key step for the complete conversion of ethanol to CO_2. The enhanced oxidation capabilities of small SnO_2 NPs on Pt also leads to increased production of the partial oxidation products acetaldehyde and acetic acid, which lowers the overall selectivity and efficiency.

Table 3.1: Experimentally observed vibrational bands and their assignments for EOR on SnO_2/Pt electrocatalysts.

Wavenumber (cm^{-1})	Identification
2343	$CO_{2(asym)}$ in solution
2050	linear $CO_{(ads)}$ on Pt
1280	C-O stretch: acetic acid
1110	ClO_4^- in solution
1045	C-O stretch: ethanol
933	(CCO) stretch: acetaldehyde

Chapter 4. Infrared Spectroscopy Investigation of Fe-Promoted Rh Catalysts Supported on Titania and Ceria for CO Hydrogenation

This work published in Catalysis Letters, 2016 DOI: 10.1007/s10562-016-1801-y

4.1 Introduction

The efficient conversion of syngas ($CO + H_2$) to oxygenates such as ethanol has become an increasingly important method for production of alternative liquid fuels [1, 14-16, 34-39]. Syngas is readily produced via gasification processes as well as natural gas reforming. As a fuel, ethanol possesses high energy density, low toxicity, and offers compatibility with existing fuel handling infrastructure [16, 38]. The continued development of catalyst materials and improved understanding as to how a catalyst converts syngas into value-added products will aid in design of future catalyst systems that are both efficient and selective to ethanol.

To date, four main groups of catalysts for the synthesis of ethanol and higher oxygenates from syngas have been developed. They are rhodium-based, molybdenum-based, modified Fischer-Tropsch catalysts and modified methanol synthesis catalysts [16]. Catalysts using Rh are particularly interesting due to their ability to perform CO dissociation, CO adsorption/insertion and hydrogenation simultaneously [14, 39-41]. On Rh based systems, CO hydrogenation to ethanol proceeds via four main reaction steps: adsorption of CO, dissociation to form adsorbed CH_x, insertion of a second CO molecule and further hydrogenation followed by desorption [37, 39]. Previous work on rhodium supported on SiO_2 shows high CO conversion rates but with high selectivity to methane at the expense of ethanol formation [14]. In order to help promote the

formation of C_{2+} oxygenate products such as ethanol, a second metal is typically added to the rhodium. Various promoters have been investigated (e.g. Fe, V, La, Li, Mn) all of which affect product distribution and CO conversion as compared to bare rhodium [15, 16, 36, 42-44]. The addition of Fe to Rh is believed to alter the product distribution by increasing the reaction barrier for the formation of methane and decreasing the barrier for ethanol formation [34].

While some control over product distribution can be gained by the addition of a metal promoter, another way to improve the selectivity for ethanol formation of the Rh catalyst is by changing the metal oxide support on which the catalyst is dispersed. Haider *et al.* showed that the activity and selectivity of both unpromoted and Fe-promoted Rh catalysts increased when the support was changed from SiO_2 to TiO_2 [15]. They attribute the change in activity to a change in the number of active sites when the support is changed. This change is believed to be a result of either increased dispersion of the FeRh particles and/or a particle-support interaction. Ceria as a metal oxide support is a popular choice for NO, CO and hydrocarbon conversion in three way catalysts due to its oxygen storage capacity and enhanced oxygen mobility [45-47]. It too, has been shown to be a promoter [48] and support [35] for ethanol formation. Changing the support for these Fe-promoted Rh catalysts from TiO_2 to CeO_2 should result in a change in selectivity due to the varying reducibility of the two supports.

A recent structural study from this group on a series of Rh/TiO_2-based catalysts has shown that the addition of Fe to Rh promotes formation of an FeRh alloy [1]. Pair distribution function (PDF) and X-ray diffraction (XRD) measurements of the FeRh catalysts after reduction under hydrogen and while under CO hydrogenation conditions show the appearance of several phases of Rh and Fe. Of them, the formation of an FeRh alloy phase correlates with an observed increase in ethanol selectivity. The amount of alloy formed is dependent on the Fe loading of the

catalyst up to ~4% wt Fe. While this study provided new insight into the roles of both Rh and Fe under CO hydrogenation, it remains unclear how alloy formation modifies the reactivity of Rh, *i.e.*, ensemble or ligand effects, and if the FeRh alloy phase is located at the surface of the catalyst.

In this work adsorption of carbon monoxide as a probe molecule is studied *via* FT-IR spectroscopy to investigate the surface structure of these Rh and FeRh particles on TiO_2 and CeO_2 supports. Not only is CO adsorption a key requirement for the formation of ethanol, but it can also be used to probe differences in the composition at the surface (*i.e.* $Rh^{0/3+}$, $Fe^{0,2+,3+}$) of these FeRh catalysts. By comparing the CO adsorption on bare Rh with the Fe-promoted Rh catalyst samples, the effect of Fe addition on the surface of the catalyst particles and the effect that a change in support has can be rationalized in regards to CO conversion efficiency and ethanol selectivity. In addition to CO adsorption, the surface of these catalysts under CO hydrogenation conditions is also studied. Identifying intermediates and products that form under reaction conditions (*i.e.* formate, acetate, alkoxy) and comparing with previously measured CO hydrogenation activity and product selectivities can provide information as to the role of Fe-addition and support reducibility on promoting ethanol formation.

4.2 Experimental

4.2.1 Catalyst preparation.

Fe-Rh/TiO_2 and Fe-Rh/CeO_2 catalysts are prepared via the incipient wetness impregnation method. Rhodium (III) nitrate hydrate ($Rh(NO_3)_3 \cdot xH_2O$) and iron nitrate nonahydrate ($Fe(NO_3)_3 \cdot 9H_2O$) are dissolved in de-ionized water and added drop-wise to P-25 titanium dioxide or cerium dioxide powder to form a paste. The metal oxide powders were pretreated at 450°C in air for 4 hours. This paste is then dried overnight at 180°C and calcined at 450°C in air for 4 hours. To produce a range of Fe:Rh loadings, the amount of iron (III) salt used was varied to produce iron weight percentages in the range of 1% to 7%, while preserving the rhodium concentration at ~2%wt. The series of FeRh catalysts synthesized will be referenced as 1FeRh, 2FeRh *etc.* A more detailed characterization of the FeRh catalysts can be seen in an earlier work [1]. Figures 4.1 shows HR-TEM images of Rh/CeO_2 while 4.2 shows a scanning transmission electron microscopy (STEM) image and size distribution for Rh/TiO_2 used in this work. From Fig 4.1 it can be seen that the Rh particles are extremely well-dispersed on the CeO_2 support, likely as cluster of several atoms. The 2.2 Å spacing corresponds to the (111) plane of Rh metal.

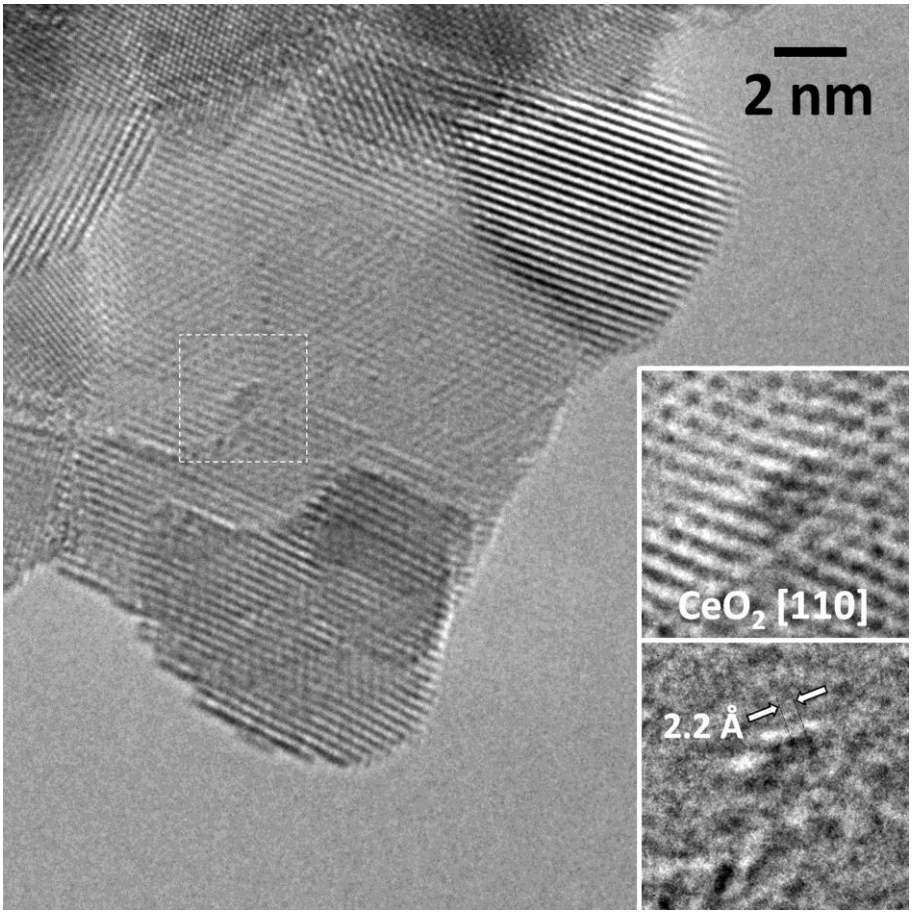

Figure 4.1: HRTEM image of Rh/CeO_2. The area enclosed in the white square is shown in the insets of the figure. The inset at the top corresponds to a filtered image obtained from the Fourier Transform image by masking the spots of the ceria crystallite support, which allows the identification of the ceria lattice of the ceria nanoparticles oriented along the [110] crystallographic direction. The inset at the bottom corresponds to the raw image after subtraction of the information contained in the spots corresponding to the ceria crystallite support, which highlights features not related to the ceria nanoparticle support.

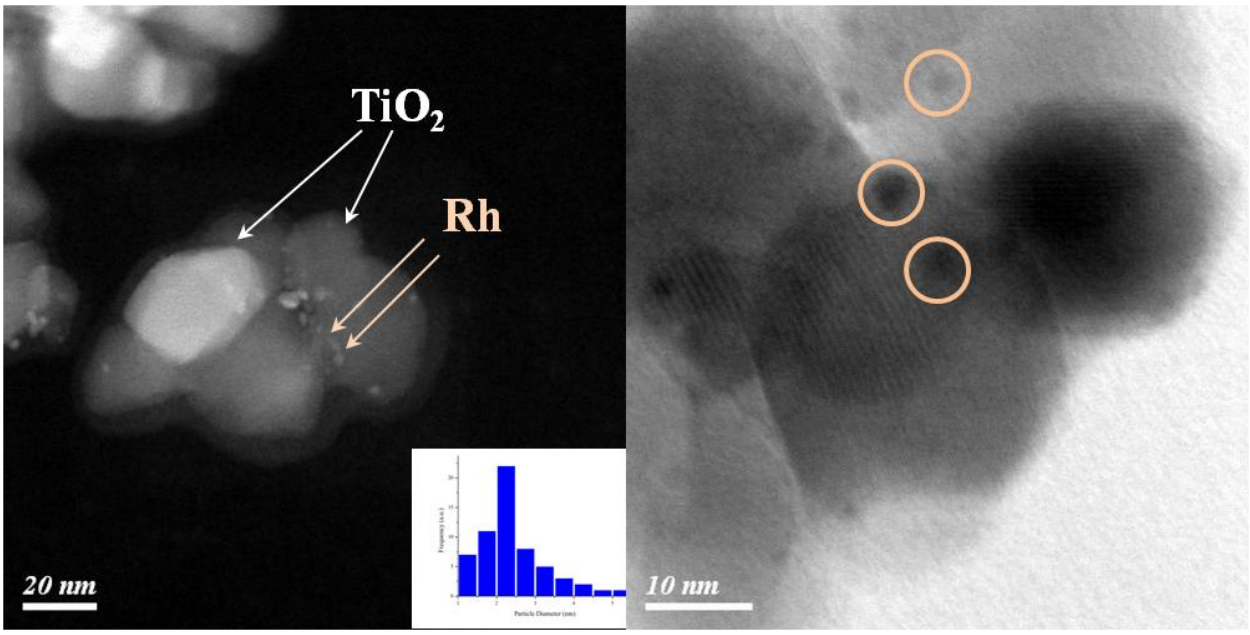

Figure 4.2: STEM image of Rh/TiO_2. The inset shows the size distribution of Rh particles. The average particle size was measured to be ~2-2.5nm over 60 particles, but as is seen from the distribution, Rh particle sizes > 5nm were also present.

4.2.2 FT-IR Spectroscopy

CO Adsorption

FT-IR spectra were collected on a Bruker Vertex 80V spectrometer using a liquid-N_2 cooled MCT detector in a homebuilt transmission cell. Figure 2.4a shows the FT-IR cell used in these experiments mounted in the sample compartment of the spectrometer and connected to a xyz-stage which allows positioning of the sample. A cross-sectional view of the cell, looking perpendicular to the direction of the IR beam, is shown in Figure 2.4b. The design of the cell is similar to that first described by Yates *et al.* [49]. The IR cell contains two ZnSe windows, which allow transmission down to < 1000 cm^{-1}. A turbomolecular pump can be used to evacuate the cell to a working pressure on the order of ~10^{-8} Torr. The cell is isolated from the sample compartment of the spectrometer and all vacuum and gas handling connections are internal. Having the cell completely isolated from the sample compartment of the FT-IR spectrometer allows the optical bench and sample compartment to be kept under vacuum (~3 Torr), eliminating the need for purging of the sample compartment with dry air or nitrogen.

For sample preparation, a small amount of catalyst is pressed into a tungsten mesh (0.2mm aperture, 64% open area, Goodfellow), which is then mounted onto a Ni sample holder that can be heated to > 450°C, as monitored with a Type K thermocouple spot-welded to the tungsten mesh. There is enough surface area on the mesh to accommodate multiple samples. The sample holder is connected to a vacuum feedthrough which is in turn connected to a xyz stage that allows for translation in all three directions. CO adsorption experiments involve the same (Fe)Rh loading on either TiO_2 or CeO_2. Hydrogen and CO gas are introduced into the cell via a manifold and regulated using mass flow controllers (MKS). Pressures for reduction, reaction and CO dosing are measured by a convectron gauge (Granville-Phillips). The catalyst is first

reduced under 1Torr of H_2 at 300°C for 20 min and then under vacuum for an additional 5 min. This reduction treatment was confirmed to result in Rh^0 by XRD in a previous study [1]. Further support for reduction was provided by the appearance of two peaks in the IR spectrum due to CO binding in a linear ($CO_{(l)}$) and bridged ($CO_{(br)}$) manner on Rh^0 sites that were not present in the as synthesized catalysts [50, 51]. After cooling to room temperature, a known pressure of CO is admitted into the cell and then evacuated. Spectra are collected at a resolution of 4 cm^{-1} with a total of 128 scans and presented as differences in absorbance. A background spectrum is collected at room temperature after reduction but prior to exposure to CO.

CO Hydrogenation

In addition to CO adsorption, the $FeRh/TiO_2$ catalysts were studied under CO hydrogenation conditions. For these experiments, catalysts were first reduced under flowing H_2 at 200 °C. After reduction, the gas flow was changed to a 2:1 ratio of $CO:H_2$ while the sample was brought up to reaction temperature. Infrared spectra during reaction were collected at temperature (180-220°C) while flowing $CO+H_2$ at a total pressure of ~800 Torr. Background spectra were collected at temperature under flowing H_2, prior to exposure to CO.

4.3 Results and Discussion

4.3.1 CO Adsorption on Rh/TiO_2 and Rh/CeO_2

The vibrational spectra in Figure 4.3 for CO adsorption on the reduced Rh-only samples exhibit four absorbance bands in the range 2150-1850 cm^{-1}. These can be assigned to characteristic CO stretching frequencies associated with different Rh binding sites identified in previous studies [51-54]. For the Rh/TiO_2 sample (Fig. 4.4a), the two peaks at 2102 cm^{-1} and 2042 cm^{-1} are assigned to the symmetric and antisymmetric stretch of CO adsorbed as a geminal-dicarbonyl ($CO_{(gc)}$) at isolated Rh^+ sites. The mechanism for formation of these Rh^+ sites involves the oxidation of small Rh^0 particles by surface hydroxyl groups of the support. These gem-dicarbonyl surface species are expected for only highly dispersed particles [50]. The two other features, a sharp peak at 2070 cm^{-1} and the broad absorbance centered at ~1900 cm^{-1}, are consistent with CO binding to Rh^0 in a linear and bridged configurations, respectively [51, 53, 55]. As the CO exposure pressure is increased, a slight shift in frequency for $CO_{(l)}$ is observed from 2061 cm^{-1} for 50 mTorr exposure to 2070 cm^{-1} for 325 Torr. This shift is consistent with dipole-dipole coupling between adsorbed CO molecules with increasing coverage [56]. The observance of bridge-bonded CO suggests the formation of larger, Rh^0 crystallites. Four distinct CO vibrational peaks are also observed for CO adsorption on Rh/CeO_2 (Fig. 4.4b), however, each peak is redshifted by ~20 cm^{-1}. The latter is consistent with a weakening of the CO bond resulting from the enhanced reducibility of CeO_2 and its effect on the electronic state of the Rh particles [48].

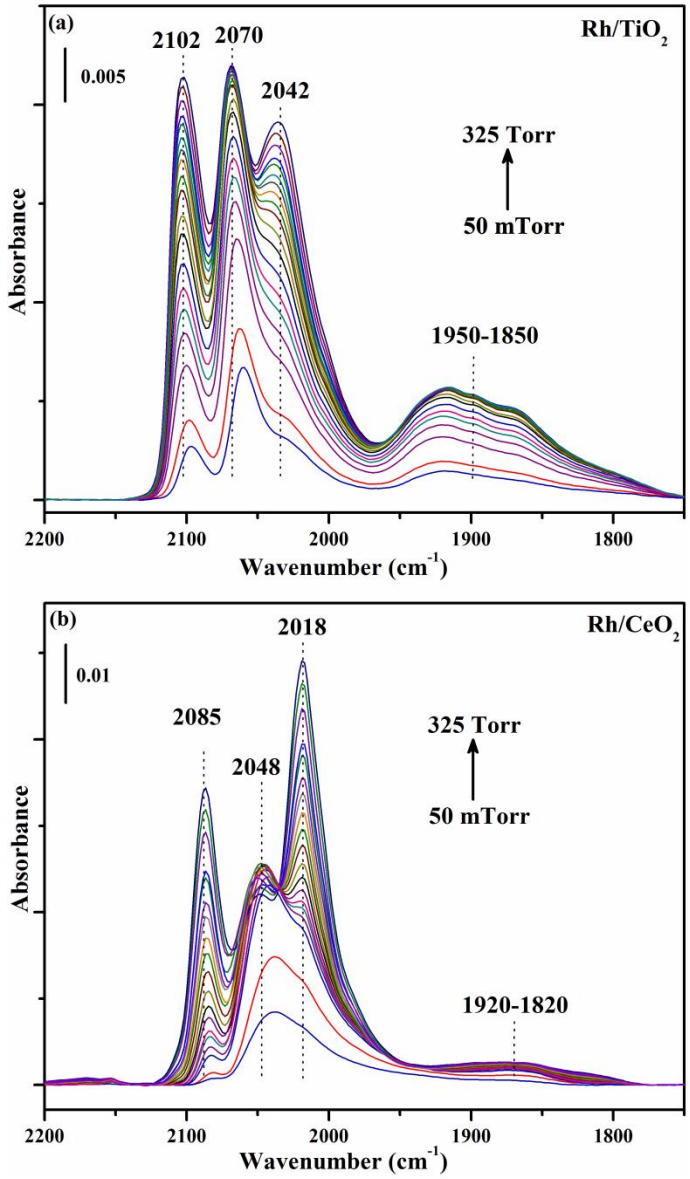

Figure 4.3: (a). Absorbance FT-IR spectra of CO adsorption on Rh/TiO_2 at 25°C at increasing CO exposure. (b) Rh/CeO_2.

Also worth noting is the difference in relative intensities of the CO vibrational bands on the titania and ceria supported samples. As the CO exposure increases on Rh/TiO_2, both $CO_{(l)}$ and $CO_{(gc)}$ signals increase. This would suggest that there are large Rh^0 particles that are resistant to oxidation and small, isolated Rh atoms or clusters on the surface as well. By comparison, the vibrational intensities for CO on Rh/CeO_2 show a much higher ratio of $CO_{(gc)}$:$CO_{(l)}$, with peaks associated with Rh^0 much smaller than on Rh/TiO_2. The enhanced formation of $CO_{(gc)}$ on the CeO_2-supported Rh suggests that the change in support promotes greater dispersion of Rh particles and a larger fraction of Rh^+ sites, likely as a result of a smaller average particle size. These support induced size variations are supported through TEM. The TEM images for Rh/TiO_2 shows particle sizes ranging from ~ 2-10 nm, whereas for Rh/CeO_2, a much higher dispersion results in Rh clusters of several atoms being identifiable (see Figures 4.1 and 4.2). Similarly, previous HRTEM results on $2FeRh/TiO_2$ and $7FeRh/TiO_2$ show an average particle size of ~2 nm that are resilient to agglomeration under CO hydrogenation [1].

4.3.2 CO Adsorption on $FeRh/TiO_2$ and $FeRh/CeO_2$

The addition of Fe to Rh/TiO_2 results in several changes to the IR spectra. Our recent structural characterization [1] of these $FeRh/TiO_2$ catalysts has identified the formation of FeRh alloy under both reduction and CO hydrogenation conditions and its importance for the formation of ethanol as a product, but could not conclusively prove the existence of *surface* FeRh alloy. Figure 4.4a shows CO absorbance as the concentration of Fe increases for $FeRh/TiO_2$ after exposure to 2 Torr of CO. Upon addition of Fe to the catalysts, changes in CO binding begin to appear. A shoulder begins to grow between 2000-1950 cm^{-1} for 2FeRh and

merges into the $CO_{(l)}$-Rh^0 peak for 3FeRh. For 1FeRh, this feature is not detectable. The peak position of $CO_{(l)}$-Rh^0 slightly redshifts for all Fe containing catalysts, suggesting a change in the local environment around Rh^0. The broad shoulder (~1970 cm^{-1}) that develops as the iron concentration increases is attributed to Fe, likely in the form of a FeRh alloy on the catalyst surface. The adsorption of CO on reduced iron particles has been studied and it is widely accepted that peaks in the range of 2040-1990 cm^{-1} are a result of CO bonded linearly to Fe^0 sites whereas bands in the range of 1980-1880 cm^{-1} are a result of bridged CO species [57-59]. Our previous XRD results showed that no fraction of the iron added to the catalyst existed as Fe metal, only as alloy, and from this it is possible to eliminate $CO_{(l)}$-Fe^0 as the source of this new feature [1]. Using this basis, the shoulder centered at ~1950 cm^{-1} is attributed to $CO_{(l)}$ and/or $CO_{(br)}$ binding to a surface FeRh alloy. Due to the electronic effect that alloying has on both Rh and Fe, it is difficult to definitively assign the peak to one particular atomic species. It is most likely a combination of sites that share Rh and Fe character. At higher concentrations of Fe, the CO-Rh features almost disappear completely, and is likely the result of the formation of an amorphous iron oxide layer at the surface, covering up surface Rh sites [1].

Similar trends in the CO vibrational spectra with increasing Fe content are observed for the FeRh/CeO_2 system shown in Figure 4.4b. The feature that appeared at 1970 cm^{-1} and is attributed to CO-FeRh is present, but less prominent than compared to the TiO_2 support. As the Fe loading is increased, the overall signal begins to decrease as the smaller Rh particles are more easily covered by iron oxide.

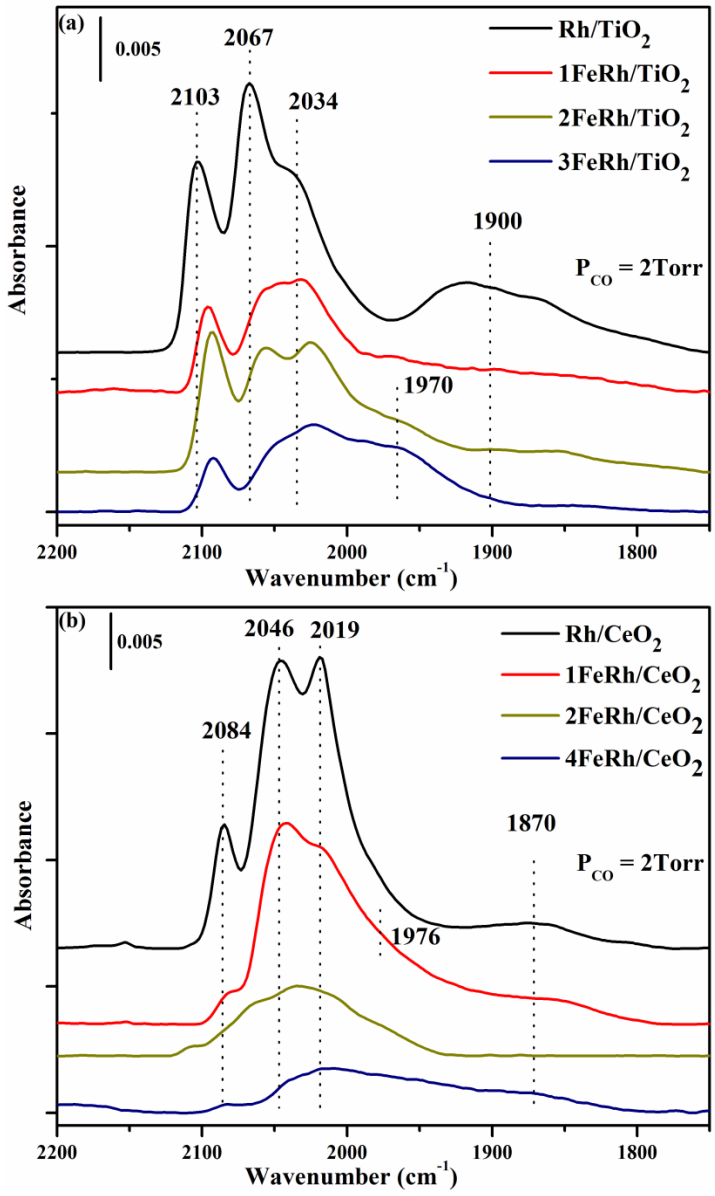

Figure 4.4: (a) Absorbance FT-IR spectra for a series of $FeRh/TiO_2$ catalysts at 25°C after exposure to 2 Torr of CO. (b) $FeRh/CeO_2$.

4.3.3 CO Hydrogenation on $FeRh/TiO_2$ and $FeRh/CeO_2$

In addition to CO adsorption experiments at room temperature, several of the FeRh alloy catalysts were studied under CO hydrogenation conditions. As noted above, intermediates such as $–CH_x$, and –C-O are expected to be formed on the catalyst surface during reaction. Several reaction temperatures in the range of 180-220°C, typical for CO hydrogenation, were chosen [60, 61]. Figure 4.5a shows spectra of Rh, 2FeRh and 4FeRh and 7FeRh on TiO_2 at 180°C after 1 hr of reaction. Peaks at 3014 cm-^{1} and 1303 cm^{-1} are due to the formation of $CH_{4(g)}$. For Rh/TiO_2, absorbance peaks due to the formation of hydrocarbons are visible at 2968 cm^{-1}, 2927 cm^{-1} and 2854 cm^{-1}. The shoulder at 2968 cm^{-1} and the peaks at 2927 cm^{-1} and 2854 cm^{-1} are ascribed to saturated alkyl species ($–CH_3$) and methylene ($–CH_2$) groups, respectively, in line with previous work.[42, 60] The broad absorbance centered around 1900 cm^{-1}, previously attributed to $CO_{(br)}$-Rh^0, can still be seen, but is greatly diminished compared to room temperature, proving that CO is still bound to the Rh particle surface at 180°C. A set of three peaks also appear at 1533 cm^{-1} and 1444 cm^{-1} and 1346 cm^{-1}. These three peaks are assigned as υ_{asym}(OCO), ν_{sym}(OCO), and $\delta_{sym}(CH_3)$ of surface bound acetate [62, 63]. There is also likely to be some contribution in the intensity of these peaks from carbonate adsorption on TiO_2 (1533 cm^{-1} and 1346 cm^{-1}) and $CH_3O–$ and/or $CH_3CH_2O–$ bending modes (1444 cm^{-1}) [42, 60, 64].

As noted above, the infrared spectrum for Rh/TiO_2 during CO hydrogenation at 180°C indicates the formation of surface-bound acetate (Fig. 4.6a), whose role in C_{2+} oxygenate formation is debated. Underwood and Bell concluded that the high stability of acetate groups on La-promoted-Rh/SiO_2 made them likely to be spectators, and only result from an accumulation of reaction products like ethanol or acetaldehyde [65]. Work on MnO-promoted-Rh/NaY

catalysts by Treviño *et al.* suggested an alternative mechanism in which acetate groups located at the metal-promoter interface are likely to be intermediates that are hydrogenated in the formation of higher oxygenates due to their proximity to H-atom spillover [66]. Since C_{2+} oxygenate products like ethanol are not expected from CO hydrogenation on Rh/TiO_2 at 180°C [14], it is not clear if acetate is an intermediate that leads to oxygenate products at higher temperatures and/or part of a secondary reaction pathway that terminates at strongly bound surface acetates.

Compared to pure Rh on TiO_2, the 2FeRh, 4FeRh and 7FeRh catalysts show some similar features that develop under CO hydrogenation conditions. Bridge bonded CO only appears on 2FeRh. At greater Fe loadings, this feature disappears, likely due to the absence of the extended Rh^0 crystallites needed to form bridge bonds. The peaks for alkyl stretches appear at 2966 cm^{-1} and 2931 cm^{-1} and there is also a marked decrease in their intensity. The change in intensity is due to the decrease in the availability of surface Rh^0, due in part to alloying with Fe. It is expected that the lack of extended surface Rh^0 decreases the CO dissociation rate, which in turn decreases the amount of C_{ads} available for hydrogenation to CH_x. The peak at 2854 cm^{-1}, attributed to an overlap in the symmetric stretch vibration of $–CH_3$ and $–CH_2$ groups on Rh/TiO_2 [42], is less prominent on the Fe-promoted samples. Instead, a new peak at 2869 cm^{-1} appears which could be due to methylene ($–CH_2$) and methyl ($–CH_3$) formation at Rh sites in contact with Fe. Once again acetates appear under reaction, as evidenced by the peak at 1444 cm^{-1}. In addition, peaks at 1566 cm^{-1} and 1369 cm^{-1} are identified as belonging to the ν_{asym}(OCO) and ν_{sym}(OCO) stretch of adsorbed formate [67]. Formate has been identified as a potential intermediate in methanol synthesis catalysts, which suggests that at a reaction temperature of 180°C, the addition of Fe to Rh/TiO_2 improves the catalyst's ability to produce methanol. This is further supported by the appearance of two peaks in the region 1120-1045 cm^{-1}, which are the C-

O stretches of mono- and bi-dentate adsorbed methoxy species [68, 69]. Formate has also been proposed as an intermediate in the formation of acetate/ethanol on Rh-MnO/NaY catalysts [70]. On Rh-MnO/NaY, formation of $–CH_x$ occurs on Rh sites through dissociative CO adsorption, while formation of formate occurs on MnO via non-dissociative CO adsorption and reaction with a surface hydroxyl. Interaction between $–CH_x$ and formate then leads to higher order oxygenate products.

At a higher reaction temperature, spectra for Rh/TiO_2 and the three $FeRh/TiO_2$ catalysts are nearly identical. Figure 4.5b shows the infrared spectra for Rh, 3FeRh and 4FeRh and 7FeRh after CO hydrogenation under flowing H_2 and CO at 220°C. Peaks associated with formate on 3FeRh, 4FeRh and 7FeRh have disappeared into only a slight shoulder of the main acetate peaks. The appearance of surface bound acetate at a temperature that ethanol formation is observed [14] supports the idea that it more likely a product of a secondary reaction pathway rather than an intermediate in the formation of ethanol in this system. Gas-phase methane is now seen as a dominant feature even in the Fe-promoted Rh/TiO_2 samples and the amount of bound $–CH_x$ has decreased compared to 180°C. The peaks from 1120-1045 cm^{-1} are still present at 220°C on the Fe-promoted samples, supporting the idea that C-O and/or C-C containing products (*i.e.* ethanol) are produced and also that they are more stable upon the addition of iron. This spectral region is

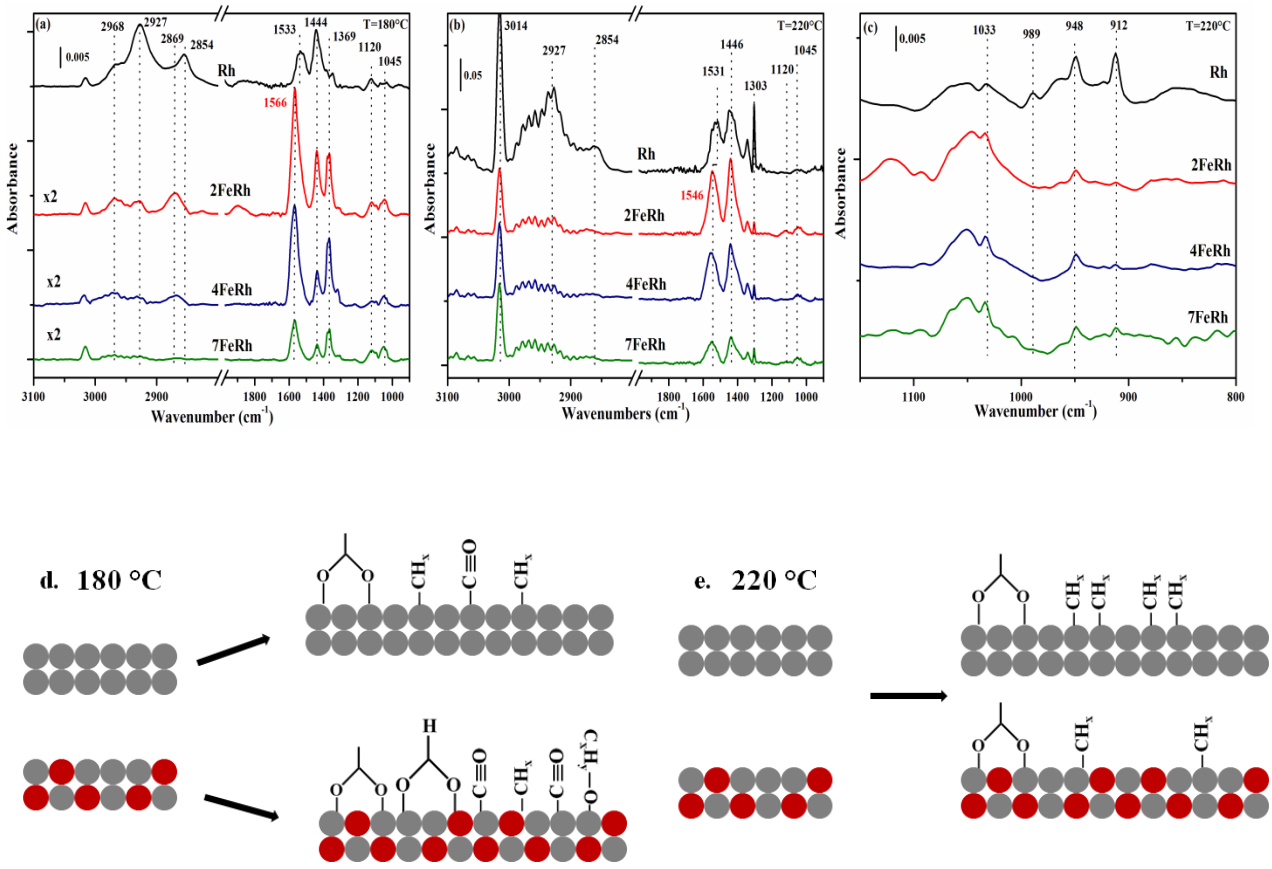

Figure 4.5: (a) FT-IR spectra for Rh, 2FeRh, 4FeRh and 7FeRh under reaction CO hydrogenation conditions (2:1 H_2:CO) at 180°C. (b). At 220 °C. For both (a) and (b) the hydrocarbon range (3100-2800 cm^{-1}) has been magnified by 2 for the iron-promoted Rh/TiO_2 catalysts. (c) close-up view of the 1150-850 cm^{-1} region of 4b. A cartoon representation of the types of surface species observed at 180 °C (d) and 220 °C (e) is shown below.

shown on an expanded scale in Figure 4.5c. Compared to spectra at 180°C, a new peak at 1033 cm^{-1} appears at 220°C and is identified as $CH_3OH(g)$ [71]. The formation of methanol also hints at another role of Fe in these systems. The increase in methoxy/methanol formation on FeRh could result from a reduction of CO dissociation and an increase in the stability of adsorbed CO. Takeuchi and Katzer studied CO hydrogenation on Rh/TiO_2 with isotopically labeled CO and concluded that due to an absence of isotope mixing in the methanol formed, production of methanol was almost exclusively through non-dissociative CO hydrogenation [72].

For Rh/TiO_2 at 220°C, 3 additional sharp peaks appear at 989 cm^{-1}, 948 cm^{-1} and 912 cm^{-1}. These are due to gas phase propene (989 cm^{-1} and 912 cm^{-1}) and ethylene (948 cm^{-1}). Comparatively, a small amount of ethylene is seen for the iron-containing catalysts. The absence of propene and the limited production of ethylene as reaction products supports the idea that the addition of iron helps decrease the production of hydrocarbons that Rh/TiO_2 favors under reaction conditions.

The evolution of the vibrational spectra as a function of Fe content and temperature seen in Figure 4.5 provides additional insight into the role of Fe on the reaction pathway and product distribution. Previously work in this laboratory has shown that under similar reaction conditions, the addition of 1% (wt) Fe to Rh/TiO_2 increases the ethanol selectivity by ~20%.[1] Further Fe addition improves selectivity to 55.6%. If the addition of Fe helped stabilize an important reaction intermediate or form a unique active site, it could be expected that spectral features would appear in the Fe-promoted samples that are not present in Rh-only sample. The fact that the IR spectra for all the catalysts show the formation of the same types of surface species under reaction conditions (Figure 4.5) suggests that the addition of Fe does not lead to a new reaction

pathway for oxygenate synthesis. Instead, the data are consistent with the hypothesis that the role of Fe addition and alloy formation is mainly to decrease the probabilities for CO dissociation and C_{ads} hydrogenation by breaking up extended Rh^0 crystallites that are responsible for the high CH_4 production seen on Rh-only systems (ensemble effect). This hypothesis is supported by reactivity studies which show that the increase in oxygenate selectivity of Fe-promoted Rh/TiO_2 catalysts is primarily due to a drastic reduction in hydrocarbon formation and a concomitant decrease in overall CO conversion [1, 15]. Our data, however, cannot discount that this is the only role of Fe. It is still possible that Fe-promotion leads to the formation of an intermediate that is simply not longed lived enough to be observable by IR spectroscopy under these experimental conditions.

The effect of changing the FeRh support from TiO_2 to CeO_2 was also investigated, specifically for the 2FeRh catalyst system. Figure 4.6 shows spectra collected after CO hydrogenation on $2FeRh/CeO_2$. Compared to $2FeRh/TiO_2$, the IR spectrum for the $2FeRh/CeO_2$ catalyst shows almost no surface bound $–CH_x$ species, which is likely due to less exposed Rh as evidenced by smaller CO adsorption (see Fig. 4.3). Methane is produced, especially at higher temperature (220°C), as seen by the CH_4(g) peaks at 3014 cm^{-1} and 1303 cm^{-1}. The –COO– region contains two broad features, centered at ~1550 cm^{-1} and ~1330 cm^{-1} which likely contain contributions from several different –COO– containing species. At 220°C, a well-resolved peak at 1428 cm^{-1} appears, which is assigned as the symmetric stretching band, ν_s(OCO) of surface bound acetate, [73] similar to that observed for TiO_2-supported 2FeRh (Fig. 4.6b). In the spectral region 1100-1000 cm^{-1}, several peaks appear at both reaction temperatures. Since $2FeRh/CeO_2$ exhibits similar CO hydrogenation selectivities as $4FeRh/TiO_2$ [2], it is likely that several of these features are due to adsorbed $CH_3O–$ and/or $CH_3CH_2O–$, but the ability of CeO_2 to adsorb

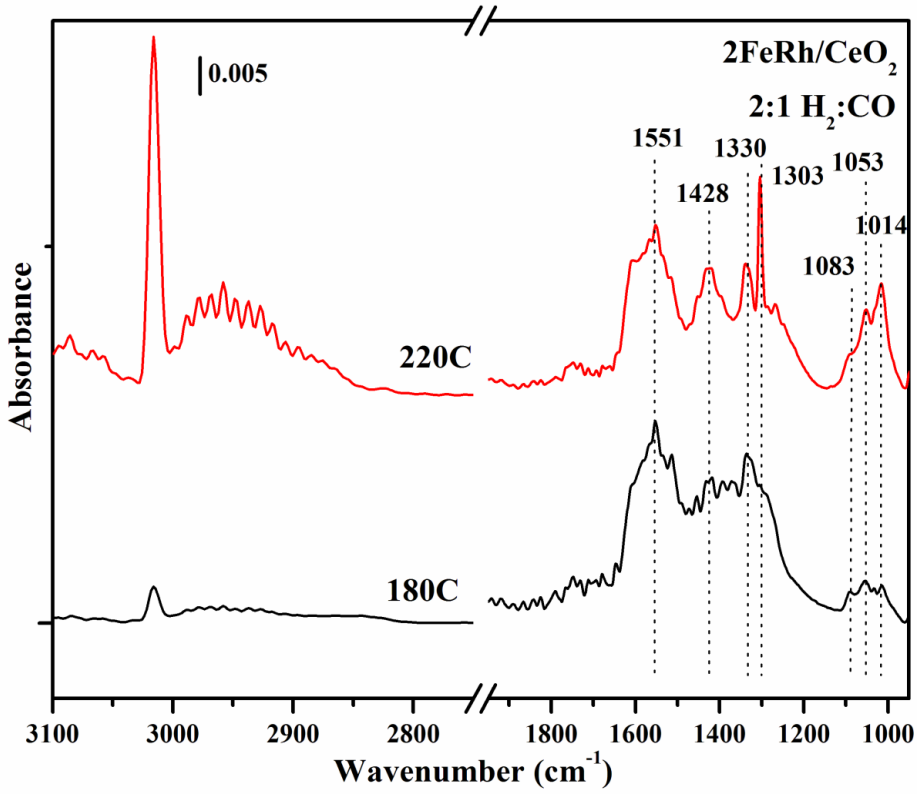

Figure 4.6: FT-IR spectra for 2FeRh/CeO_2 under CO hydrogenation conditions at 180° (black) and 220°C (red).

CO (1028 cm^{-1} and 1062 cm^{-1}) and CO_2 (1011 cm^{-1} and 1045 cm^{-1}) [74, 75] at these reaction temperatures makes conclusive identification of the peaks difficult. A summary of all the vibrational bands observed for the supported Rh and FeRh catalysts and their assignments are given in Table 4.1.

4.4 Summary

CO adsorption on a series of Rh-based CO hydrogenation catalysts was investigated using FT-IR spectroscopy. CO absorbance results for reduced Rh/TiO_2 and Rh/CeO_2 exhibit characteristic vibrational bands that support the existence of both Rh^0 and Rh^+ on the surface. Compared to Rh/TiO_2, the Rh/CeO_2 catalyst results in a higher $CO_{(gc)}$:$CO_{(l)}$ ratio, showing that changing the support from TiO_2 to CeO_2 increases the dispersion of the Rh particles. Adding Fe to the Rh/TiO_2 and Rh/CeO_2 results in the appearance of a new CO vibrational band which is identified as CO adsorbed on Rh that is alloyed with Fe, suggesting that the FeRh alloy exists at the surface of these catalysts. Under CO hydrogenation conditions, the observed IR spectra for Rh/TiO_2 indicate the formation of CH_4 as well as the presence surface bound products such as methylene and acetate. At low reaction temperatures, Fe addition promotes the formation of formate and methoxy, intermediates in methanol formation. At higher reaction temperatures, formate and methoxy features disappear, and the vibrational spectra for Fe-containing catalysts appear similar to that of bare Rh/TiO_2, albeit with much lower CH_4 formation. Similar intermediates were seen under CO hydrogenation for $2FeRh/CeO_2$, but due to the complicated spectra resulting from CO/CO_2 adsorption on the CeO_2 support, definitive conclusions about the effect of the support on intermediate formation prove difficult. Overall, the results presented here further confirm the role of Fe which is to regulate CH_4 production by breaking up larger Rh^0 surface regions through alloy formation to FeRh (ensemble effect).

Table 4.1: Experimentally observed vibrational bands and their assignments for supported Rh and FeRh catalysts.

Wavenumber (cm^{-1})	Identification
3014 and 1303	$CH_4(g)$
2968	ν_{asym} $–CH_3$
2927	$–CH_2$
2869	$–CH_2$ / $–CH_3$ on Rh-Fe sites
2854	ν_{sym} $–CH_3$
2102/2042	$CO_{(gc)}$ on Rh^+
2070	$CO_{(l)}$ on Rh^0
~1950	$CO_{(br)}$ on FeRh
~1900	$CO_{(br)}$ on Rh^0
1566/1369	ν_{asym} and ν_{sym} (OCO) formate
1533/1444	ν_{asym} and ν_{sym} (OCO) acetate
1346	δ_{sym} CH_3 acetate
1120-1045	C-O stretch of mono- and bidentate alkoxy
1033	$CH_3OH_{(g)}$
989/912	propene $_{(g)}$
948	ethylene $_{(g)}$

Chapter 5. *In Situ* Photocatalysis on P-25 TiO_2: Observation of Photogenerated Electrons and Photooxidation of Acetaldehyde.

5.1 Introduction

Rather than using an applied potential or increased temperature to drive the conversion of reactants into products, photocatalysts harness power from light to generate energetic electrons and holes capable of performing chemistry. Figure 5.1 illustrates some of the fundamental processes of semiconductor photoexcitation. When light of a certain wavelength (λ) with energy greater than the band gap of the material interacts with the surface of a photocatalyst it can generate electron/hole (e^-/h^+) pairs. These pairs are formed when an electron from the valence band of the semiconductor is promoted to the conduction band. This energetic electron can be transferred to adsorbed molecules and act as a reductant. Similarly, the hole, which remains in the valence band, can interact with an adsorbed molecule as an oxidant. Being able to generate electron-hole pairs while using light and keeping the e^- and h^+ separate for long enough to become involved in a reaction are two important considerations in the continued development of photocatalysts. TiO_2-based photocatalysis has been extensively studied [76-78]. The band gap is ~3.2 eV for anatase and 3.05 eV for rutile, both of which require UV irradiation to generate electron/hole pairs. Work has been done on both rutile (110) single crystal surfaces [79-81] and on powder catalysts [76, 77, 82]. On single crystal rutile (110) surfaces, photooxidation of small organics like acetone is believed to proceed after the formation of a acetone-diolate complex [83]. This complex is formed after the interaction and thermal activation of acetone and adsorbed oxygen. In the absence of O_2, no $\cdot CH_3$ photo-products are observed, confirming the importance of O_2 in these reactions. Less extensive work has been done on anatase surfaces, in large part due

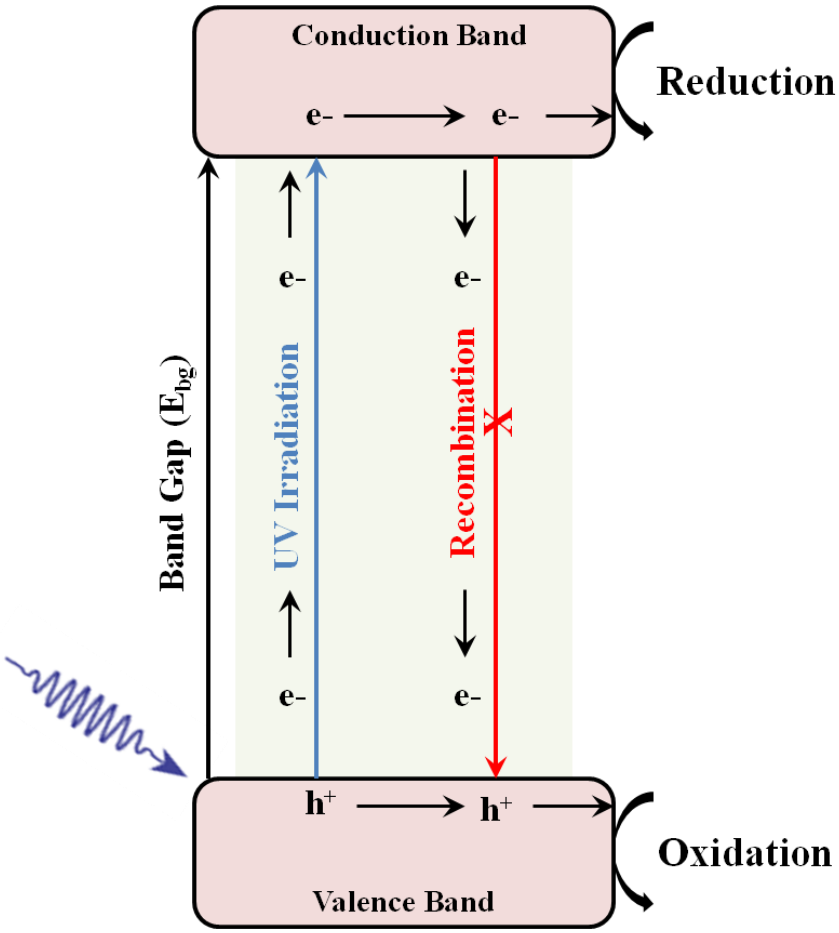

Figure 5.1: Band gap excitation in semiconductor photocatalysts. Upon absorption of a photon where $E_{ph}>E_{bg}$, an electron is promoted from the valence band to the conduction band. If recombination of the e^- and h^+ can be prevented, the electrons and holes can move to the surface and become involved in reduction and oxidation reactions.

to the lack of availability of pure crystals. Work on anatase (001) thin films grown using molecular beam epitaxy for trimethyl acetate photodecomposition show similar photocatalytic activity when compared to the rutile TiO_2 (110) surface [84]. These molecules (ketones, alcohols, aldehydes) serve as models of toxic pollutants that are found in the environment. In the presence of O_2 and UV light, TiO_2 is capable of decomposing these molecules, sometimes mineralizing them completely to CO_2. Much is known about how TiO_2 functions as a photocatalyst, but there still remain many unanswered questions as to the roles of electrons and holes in these reactions.

In order to further explore semiconductor photocatalysis, a vacuum compatible UV/Vis fiber optic coupler that allows for irradiation and excitation of a semiconductor powder photocatalyst while probing the surface of the catalyst using FT-IR spectroscopy was designed. This *in situ* approach lets us study the effect of UV irradiation (and electron/hole pair generation) on the semiconductor surface. As a proof of concept, TiO_2 was the initial semiconductor chosen. Photogenerated electrons in TiO_2 show a characteristic IR absorption that can be used to confirm photoexcitation. This MIR absorbance is rather broad and featureless in the range of 4000 cm^{-1} to 1000 cm^{-1} [85, 86]. This process can be seen in Figure 5.2. The absorptions are due to either (c) excitation of a trapped electron back to the conduction band [87] or (d) absorption of IR radiation from free electrons within the conduction band [88]. After characterizing the response of TiO_2 to irradiation, it becomes possible to then study photooxidation of a model system. By introducing an organic molecule, in this case d_4-acetaldehyde, it becomes possible to study fundamental photooxidation processes such as the reaction pathway and any surface bound intermediates that may form on TiO_2. The formation of an active acetaldehyde-diolate complex and formation of surface bound formate is shown in Figure 5.3.

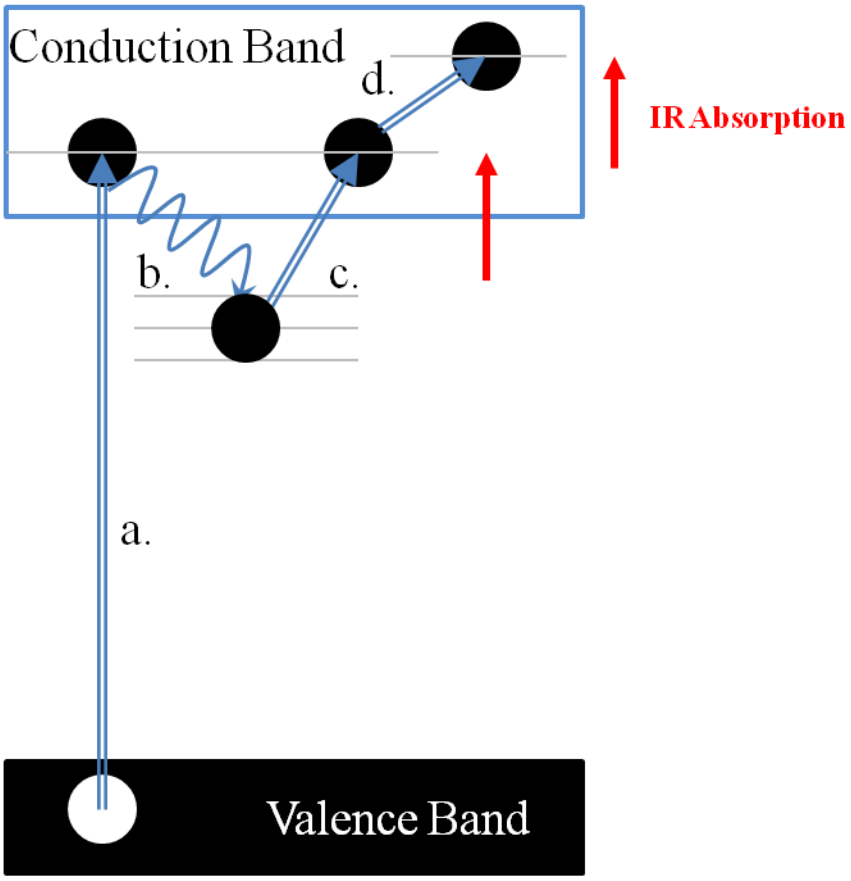

Figure 5.2: Electronic transitions occurring in TiO_2: (a) Generation of electron/hole pair by absorption of a photon with energy $>E_{bg}$. (b) Transition of an e^- from the conduction band to a shallow trap. (c). Excitation of an e^- from a shallow trap back to the conduction band. (d). Absorption of IR radiation of free electrons within the conduction band. Processes (c) and (d) are observable as broad featureless absorption in an IR spectrum.

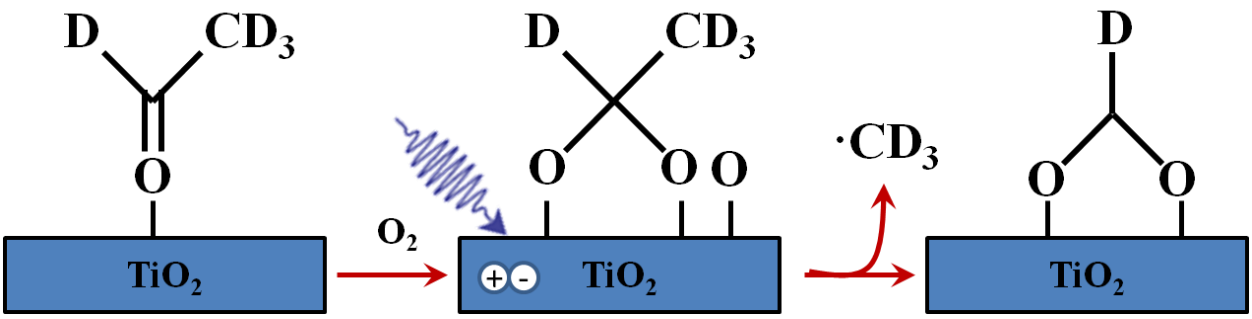

Figure 5.3: Formate formation from acetaldehyde photooxidation on TiO_2 (110). The formation of the diolate species in the second panel requires the presence of O_2 and thermal activation. Upon further UV irradiation, $\cdot CD_3$ radicals are ejected, leaving formate on the surface.

5.2 Experimental

The experimental design is discussed in detail in sections 2.2.2 and 2.2.3. Briefly, a home-built FT-IR reactor cell is mounted to the sample compartment of Bruker Vertex 80V FT-IR spectrometer. This reactor cell is capable of being evacuated to a pressure > ~10^{-8} Torr by a turbomolecular pump. The cell is also connected to a gas manifold that controls the flow of reactant gases. Liquid samples are held in a glass vial connected in-line with the gas handling system. Prior to use d_4-acetaldehyde was subjected to several LN_2 freeze-thaw cycles to remove any impurities. Deuterated acetaldehyde is used in order to differentiate $–CD_3$ groups from any potential hydrocarbon contamination. For dosing, d_4-acetaldehyde vapor was leaked into the cell until a total pressure of ~15 Torr was reached.

The P-25 TiO_2 sample was used as received. P-25 contains roughly 75% anatase and 25% rutile with an average particle size of ~20nm. It was mounted on a tungsten mesh using a hydraulic press @ 20,000 psi. It was then mounted to the same nickel clamps used in the FeRh CO hydrogenation experiments. The only difference is that the sample holder is rotated 45° with respect to the incoming IR beam, so that a large section of the TiO_2 surface can be irradiated by the incoming UV light. Prior to any experiments, the TiO_2 sample was cleaned by heating to 300 °C in 1 Torr O_2 for 30 minutes to remove any contamination from exposure to air.

Light was provided by 2 LED diodes that output at 365 nm and 515 nm. These diodes are coupled to the cell via a 1000 μm fiber optic cable. This cable is connected to a UHV-compatible fiber optic coupler, which is connected to a collimator. This allows for focused irradiation of the TiO_2 sample with light that possesses enough energy for band gap excitation (365nm) or light that does not (515nm).

5.3 Results and Discussion

5.3.1 Photogenerated Electrons in TiO_2

In order to confirm that the experimental geometry allowed simultaneous UV irradiation with FT-IR spectrum collection, the TiO_2 support was irradiated under vacuum. Under vacuum, photexcited electrons are longer lived, as the concentration of electron scavengers, namely O_2, is much less then under atmospheric conditions. Spectra collected of TiO_2 irradiated by 365nm UV light can be seen in Figure 5.4. As mentioned above, irradiation of a semiconductor leads to the formation of electron-hole pairs. The electrons are promoted to the conduction band and after promotion they begin to decay. They can become trapped in slightly lower energy levels, which correspond to defect sites in the semiconductor and they can be excited to high energy levels within the conduction band. These two transitions, illustrated as (c) and (d) in Fig. 5.2, correspond to energy in the MIR range. The absorption of MIR radiation shows as a broad absorption from 4000 – 1000 cm^{-1} . The appearance of this feature only under 365 nm UV (no change in absorption is seen for 515 nm) confirms that the UV/Vis light coupler and sample are arranged properly so that the TiO_2 surface can be probed via IR while being irradiated. Small peaks in the range of 1700-1300 cm^{-1} can be seen in Figure 5.4 as the irradiation time increases. These peaks are due to the loss of surface bound H_2O (negative peak at ~1615 cm^{-1} and the formation of several different CO_x species, likely as a result of slight oxidation of surface hydrocarbons. By monitoring the absorbance change at any wavenumber, changes in the concentration of photoelectrons can be inferred. The dashed line at 1900 cm^{-1} shows where changes in absorbance were monitored upon switching the UV on/off and addition of two known electron scavengers (O_2 or SF_6) to the reactor cell. These changes over time can be seen in Figure 5.5.

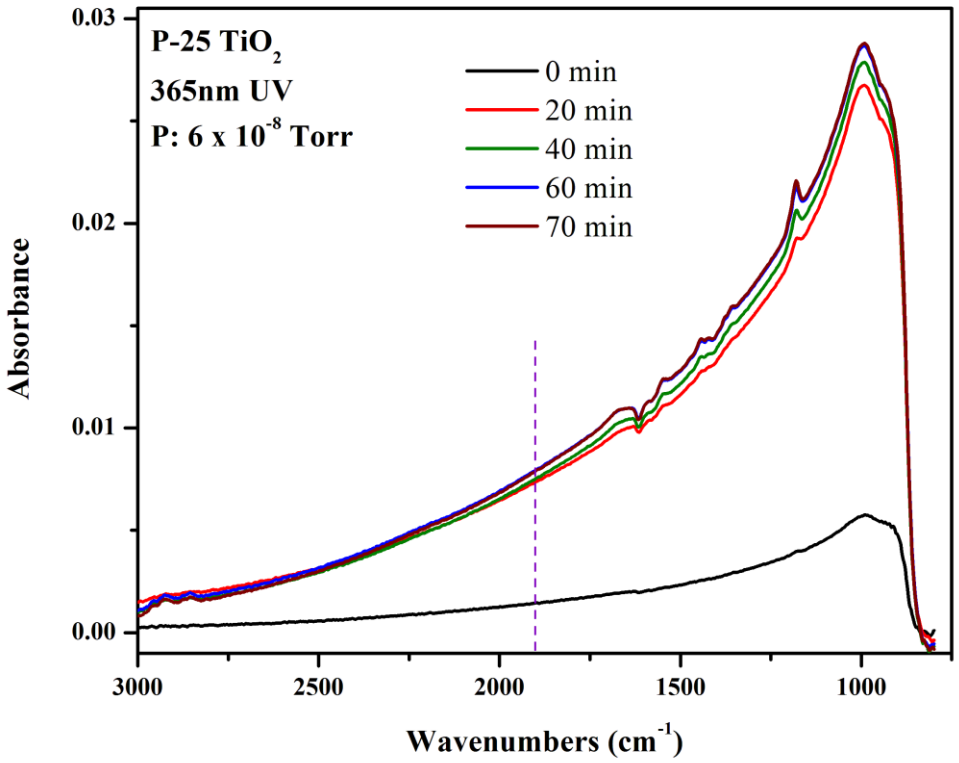

Figure 5.4: IR spectra of P-25 TiO_2 under 365nm UV irradiation. The dashed line is at 1900 cm^{-1} and is used as a reference point to measure changes in electron absorption.

From Fig. 5.5a it can be seen that there is an immediate increase in intensity after the UV is turned on that begins to plateau after 40 minutes. After the addition of 500 mTorr of SF_6, the electron signal was immediately quenched, even though the UV light remained on. After the SF_6 is evacuated from the cell, intensity returns again, although not to the extent that was seen initially. The decrease in intensity is likely due in part from residual SF_6 that may have adsorbed on the TiO_2 and from impurities introduced during gas dosing. Once the UV light is turned off, a gradual decay in signal towards baseline was observed. It is worth noting that the addition of SF_6 removed the electron build up much more quickly than simply removing the irradiation. Similar behavior can be seen in Fig. 5.5b for CD_3CDO adsorbed on TiO_2. The addition of 125 mTorr of SF_6 to irradiated TiO_2 resulted in a sharp decrease in signal intensity which can be recovered again once the SF_6 is evacuated from the reactor cell. Instead of the final step being removal of UV irradiation, 125 mTorr O_2 was added to the reactor cell. The admission of O_2 resulted in a decrease in electron intensity more quickly than a similar pressure of SF_6 and faster than what could be measured by the spectrometer. From these experiments it becomes clear that the generation and recombination of electrons in TiO_2 can be monitored using FT-IR spectroscopy. Addition of an electron scavenger, SF_6 or O_2, removes the electrons faster than just removing the UV irradiation does. The ability of SF_6 to perform this task comparably to O_2 provides a novel way to help determine the role of holes in driving photooxidation reactions by being able to remove excess electrons while creating additional holes in the absence of O_2.

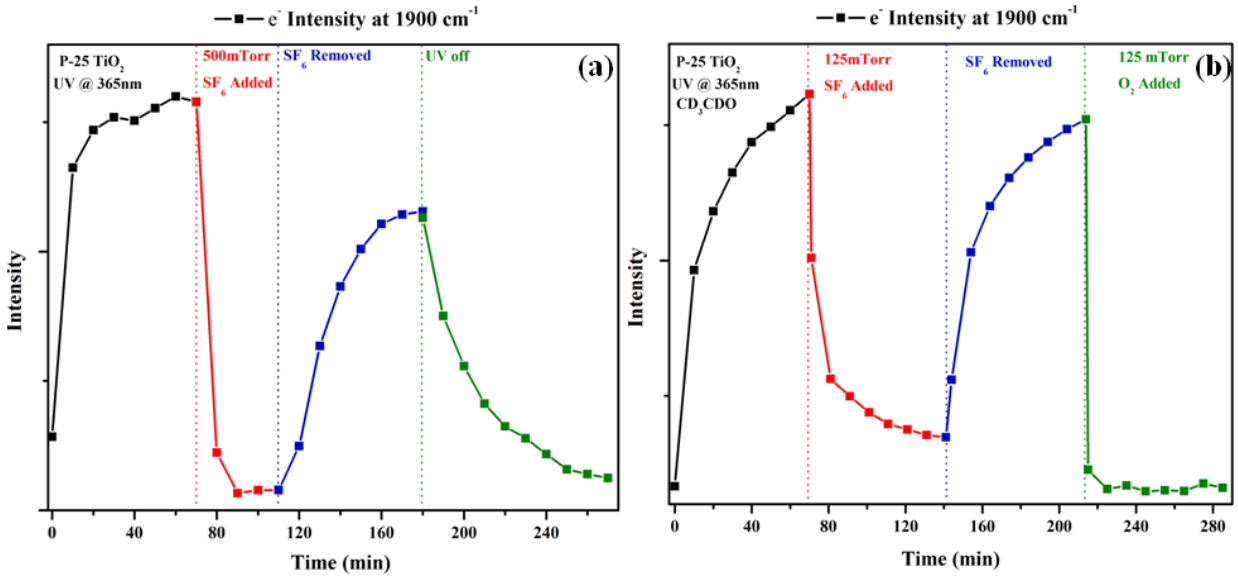

Figure 5.5: Plots of photoelectron response measured at 1900 cm^{-1} vs. time for (a) bare TiO_2 and (b) CD_3CDO adsorbed on TiO_2.

5.3.2 Photooxidation of d_4-acetaldehyde on TiO_2

After characterizing the response of TiO_2 to UV irradiation and the addition of O_2 and SF_6 to the reactor cell, photooxidation of acetaldehyde was studied. Oxidation of acetaldehyde on single crystal rutile (110) TiO_2 involves the activation of acetaldehyde on the surface as a diolate. Upon UV irradiation, a C–C bond is broken, and CH_3 radicals are ejected from the surface. The remaining surface bond –CHO rearranges to formate [81]. An IR spectrum of d_4-acetaldehyde adsorbed on TiO_2 is shown in Figure 5.6. The left panel shows a single negative peak centered at 3667 cm^{-1} upon adsorption of acetaldehyde [82]. This feature is due to a decrease in surface hydroxyl coverage on TiO_2. As acetaldehyde adsorbs, surface hydroxyls are displaced. The right panel shows the spectral features attributed to acetaldehyde. The set of three peaks at 2221, 2130 and 2067 are assigned to the ν_{as} (CD_3), νs (CD_3) and ν (CD), respectively of adsorbed acetaldehyde [89, 90]. The sharp peak at 1629 cm^{-1} is from a carbonyl (C=O) vibration, likely a combination of acetaldehyde and 2-butenal, which readily forms as a condensation product of acetaldehyde at room temperature [89], while the peak at 1149 cm^{-1} is due to the C-C bond. The series of peaks in the region around the peak at 1052 cm^{-1} are due to δ_s and δ_{as} modes of CD_x groups. At room temperature it is clear that there is likely to be both acetaldehyde and 2-butenal present on the TiO_2 surface.

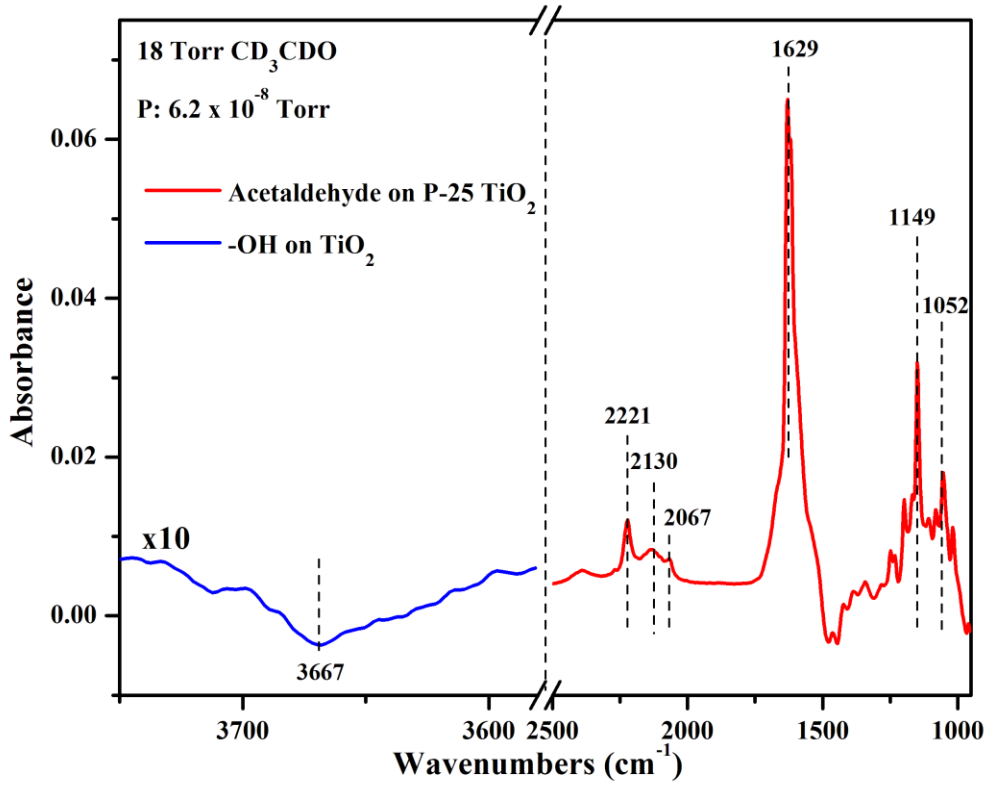

Figure 5.6: FT-IR spectrum of CD_3CDO adsorption on P-25 TiO_2. The left (blue) panel shows the hydroxyl region of TiO_2 while the right (red) panel shows adsorbed acetaldehyde features.

Figure 5.7 shows the formation of photooxidation products under different experimental conditions. The black trace is 365 nm UV light and 1 Torr of O_2 in the reactor cell. The blue trace shows the same CD_3CDO+TiO_2 @ 365 nm UV, but using SF_6 instead of O_2. The red trace used 365nm nm light *only* and can be considered a control experiment. After 1 hr of irradiation many acetaldehyde features decrease. Negative peaks at 2229 (–CD_3), 1631 (C=O) and several peaks <1250 cm^{-1} are all due to removal of CD_3CDO. This decrease in signal likely contains contributions from photoreaction and photodesorption. The fact that the 515 nm irradiated sample showed a large decrease in CD_3CDO signal suggests that the decrease cannot be attributed solely to reaction. Compared to Fig 5.6, there are clearly two peaks seen in the carbonyl region of Fig 5.7. Upon adsorption at room temperature, acetaldehyde can undergo aldol condensation to form 2-butenal [91]. It is possible that the peak at 1614 cm^{-1} is from a combination of the C=O and C=C vibrations from 2-butenal.

The two new features that appear after irradiation are centered at 1544 and 1347 cm^{-1}. These two broad features are tentatively assigned to the ν_{as} and ν_s of –COO– groups from formate on the TiO_2 surface [67, 69]. The observance of the formation of formate is in agreement with previous work on TiO_2 (110) single crystals and powder samples [81, 89]. It is believed that formate is formed after the removal of a $CD(H)_3$ group. The remaining CDO rearranges on the surface to yield formate. While it was not detected in this experiment, ultimately the adsorbed formate should be converted to CO_2 and desorb from the TiO_2 surface.

Perhaps the most surprising result from this introductory work on photooxidation of acetaldehyde was that replacing O_2 with SF_6 also resulted in the observation of formate. While the signal was not as intense as that for O_2, using an electron scavenger that conclusively is not directly involved in the reaction could be helpful in determining the roles of electrons and holes

in these photooxidation processes. On TiO_2 (110), O_2 is needed to activate adsorbed acetaldehyde to form a diolate, which is then active for C–C bond cleavage and $\cdot CH_3$ ejection. In the absence of O_2, no formate is produced. While the IR absorbance observed for acetaldehyde + SF_6 is much weaker than that with O_2, the observance of photocatalytic activity in the absence of O_2 suggests that on powder catalysts the formation of an activated species may not be necessary or the reaction pathway is different.

The active species for the photooxidation of ethanol on TiO_2 powder are $\cdot OH$ and h^+, depending on the EtOH surface coverage [69]. Holes that become trapped at surface hydroxyls can form $\cdot OH$, which can then remove an H atom from either the α or β carbon of EtOH/EtO^- forming water. H_2O molecules can then react with holes, forming additional $\cdot OH$. This reaction step leads to CH_3CHO, CH_2CH_2O, and ultimately formate and formic acid. Coronado *et al.* studied photooxidation of acetone on TiO_2 and concluded that acetone forms both 2 carbon and 1 carbon species on the surface, breaking a C-C bond, after interacting with photogenerated charge carriers and that both acetate and formate form under irradiation [82].

The formation of formate with SF_6 shows that on P-25 TiO_2, it is possible that O_2/SF_6 has a role as a surface charge manager. Recent work on CO adsorption on Au/TiO_2 showed that upon physisorption of SF_6 on TiO_2, a blueshift in the frequency of CO–Au was observed [92]. This shift was attributed charge transfer from TiO_2 defect sites to SF_6 and from Au to TiO_2. It is possible that on TiO_2 powder, two parallel photooxidation reaction pathways exist. Formation of the diolate complex and an $h^+/\cdot OH$ mediated pathway that both terminate at adsorbed formate. Long term, O_2 may be necessary to provide additional O-atoms for oxidation product formation, but in the timeframe of this study, there are enough free surface O atoms to facilitate the formation of formate.

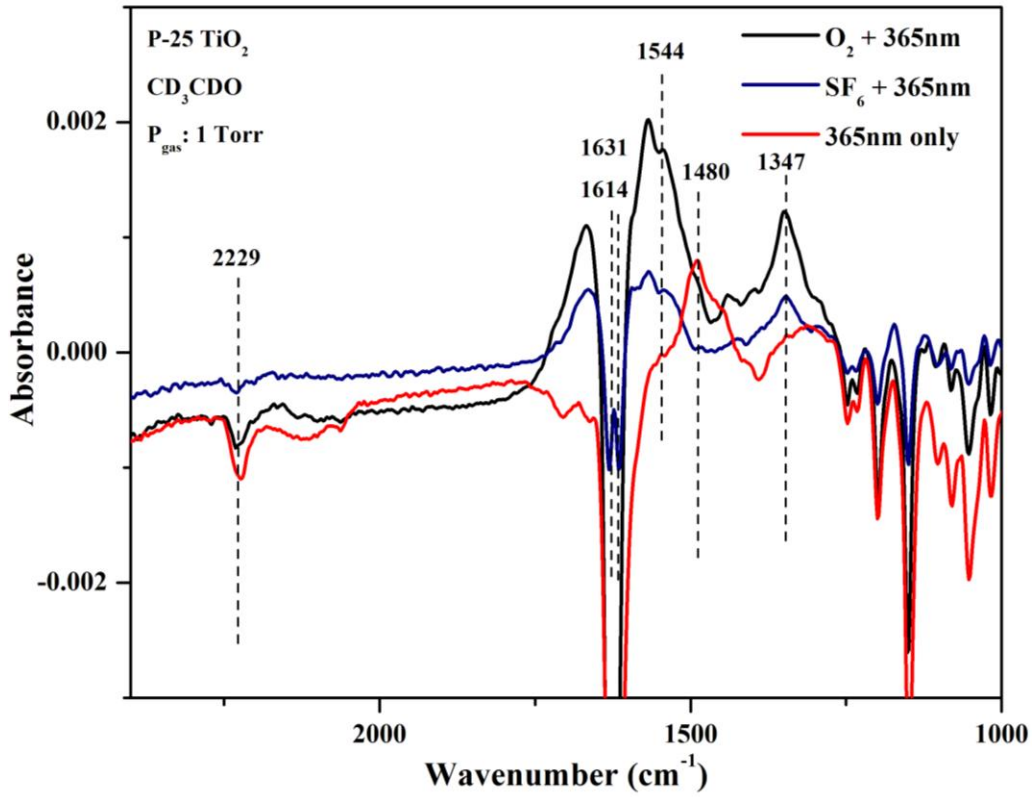

Figure 5.7: Photooxidation of CD_3CDO on TiO_2. TiO_2 was irradiated in a background pressure of 1 Torr of gas. The black trace is after 1 hour of 365 nm irradiation in O_2. The blue trace is 365 nm in SF_6. The red trace shows CD_3CDO in the presence of only 365nm UV irradiation.

5.4 Summary

Upon absorption of UV light with $E_{ph} > E_{bg}$ electron-hole pairs are generated in semiconductors like TiO_2. These energetic electrons and holes are capable of driving chemical reactions like photooxidation. These photoelectrons can be observed *in situ* by FT-IR spectroscopy as promotion from trap states back to the conduction band and intraband transitions within the conduction band are comparable in energy to the MIR photons used in FT-IR spectroscopy. This broad absorption feature can be used as a handle to study changes in electron concentrations in different environments. The addition of an electron scavenger like O_2 or SF_6 immediately quenches these free electrons more quickly than removing the UV source.

By combining an *in situ* transmission cell with a vacuum compatible UV/Vis fiber optic coupler, monitoring the photooxidation of acetaldehyde on TiO_2 is possible. It is seen that upon irradiation with 365 nm UV light in the presence of O_2, acetaldehyde is converted to formate on the TiO_2 surface. This is in agreement with previous work on the photooxidation of acetaldehyde. Replacing O_2 with SF_6 also resulted in the appearance of formate, but in a smaller amount compared to O_2. The ability to remove excess electrons and drive reactions without the presence of O_2 can lead to improved understanding of the roles of electrons and holes in this reaction. In the future, the degree of oxidation and reduction of the TiO_2 support and how it affects photooxidation will be investigated.

Table 5.1: Experimentally observed and assigned vibrational frequencies for acetaldehyde photooxidation on TiO_2.

Wavenumber (cm^{-1})	Identification
3667	$-OH_{(s)}$ TiO_2
2221	ν_{asym} $-CD_3$
2130	ν_{sym} $-CD_3$
2067	ν CD
1629	C=O acetaldehyde
1614	C–C/C=O 2-butenal
1544	ν_{asym} –COO– formate
1347	ν_{sym} –COO– formate
1149	C–C acetaldehyde
1052	δCD_3 acetaldehyde

Chapter 6. Conclusions and Future Directions

The results presented in this dissertation illustrate a few of the many applicable uses of *in situ* FT-IR spectroscopy in heterogeneous catalysis. Being able to study the mechanism of important reactions such as ethanol electro-oxidation, CO hydrogenation and photooxidation by developing unique catalyst materials, reactor cells, and instrumentation can provide important information as to how the system works as well as how to positively influence the design of future materials.

Ideally, the efficient electrochemical oxidation of ethanol at Pt electrodes would result in the formation of CO_2. However, it's well-known that CO binds to Pt strongly and eventually poisons the catalyst. The addition of SnO_2 nanoparticles to the Pt surface was shown electrochemically to enhance the current generated under EOR conditions as well as improve the stability and lifetime of the pc-Pt electrode. Creating a spectroelectrochemical reaction cell made it possible to study the products of the reaction and any intermediates bound to the pc-Pt surface helped to clarify the role of SnO_2 in this reaction. Through *in situ* IRRAS, it was shown that SnO_2 enhances both the partial oxidation products of EOR, as well as lessens the potential needed to remove strongly bound CO from the Pt surface. Looking ahead, this cell can be adapted and used to help determine how reactions proceed on other electrocatalytic systems like ultrathin metal nanowires and how their enhanced surface area improves activity compared to more traditional metal nanoparticle shapes.

Previous work on FeRh catalysts supported on TiO_2 and CeO_2 for CO hydrogenation showed that under reaction conditions a FeRh alloy phase was formed, and that the appearance of this phase correlated with an increase in ethanol selectivity. The previous work was a

combination of *in situ* XRD and PDF as well as reactivity studies using gas chromatography. Being able to study the surface of these catalysts by mimicking reaction conditions in the FT-IR reactor cell made it possible to observe differences in CO binding with different Fe loadings as well as the influence of the support on the electronic state of Rh. On the surface of these Fe-promoted materials no unique surface bound intermediate was observed giving further evidence to the idea that the role of Fe is simply to slow down CO dissociation and CH_4 formation at Rh sites, which indirectly promotes ethanol selectivity. Going forward this reactor cell will continue to be used to study future CO hydrogenation catalysts with alternative promoters including Mn, K and Li. Both Mn and the alkalis are known to alter reactivity in Rh-based systems, and looking at them *in situ* under reaction conditions via transmission FT-IR spectroscopy could help to explain the differences in product distribution.

Similar experiments can be envisioned in the future for the photochemistry cell designed and tested in this dissertation. Preliminary results have shown that the design of the UV/Vis light feedthrough and orientation of the sample mount results in overlap of the two beams. Preliminary experiments with O_2 and SF_6 illustrate that the kinetics of electrons generated by UV irradiation can be measured and preliminary photooxidation experiments with acetaldehyde show that just as is the case for thermal experiments, surface sensitive measurements of under reaction conditions can be made and surface bound products and intermediates can be observed. Ideally, any semiconducting material that can generate electron/hole pairs under UV irradiation can be studied for any number of photo-oxidation or photo-reduction reactions.

References

1. Palomino, R.M., J.W. Magee, J. Llorca, S.D. Senanayake, and M.G. White, *The effect of Fe-Rh alloying on CO hydrogenation to C_{2+} oxygenates.* Journal of Catalysis, 2015. **329**: p. 87-94.
2. Palomino, R.M., *In situ characterization of promoted Rh nanocatalysts during CO hydrogenation*, in *Chemistry*. 2015, Stony Brook University: Stony Brook University.
3. Li, M., W.P. Zhou, N.S. Marinkovic, K. Sasaki, and R.R. Adzic, *The role of rhodium and tin oxide in the platinum-based electrocatalysts for ethanol oxidation to CO_2.* Electrochimica Acta, 2013. **104**(0): p. 454-461.
4. Kowal, A., M. Li, M. Shao, K. Sasaki, M.B. Vukmirovic, J. Zhang, N.S. Marinkovic, P. Liu, A.I. Frenkel, and R.R. Adzic, *Ternary Pt/Rh/SnO_2 electrocatalysts for oxidizing ethanol to CO_2.* Nature Materials, 2009. **8**(4): p. 325-30.
5. Kavanagh, R., X.M. Cao, W.F. Lin, C. Hardacre, and P. Hu, *Origin of low CO_2 selectivity on platinum in the direct ethanol fuel cell.* Angew Chem Int Ed Engl, 2012. **51**(7): p. 1572-5.
6. Antolini, E. and E.R. Gonzalez, *Effect of synthesis method and structural characteristics of Pt-Sn fuel cell catalysts on the electro-oxidation of CH_3OH and CH_3CH_2OH in acid medium.* Catalysis Today, 2011. **160**(1): p. 28-38.
7. Colmenares, L., H. Wang, Z. Jusys, L. Jiang, S. Yan, G.Q. Sun, and R.J. Behm, *Ethanol oxidation on novel, carbon supported Pt alloy catalysts - Model studies under defined diffusion conditions.* Electrochimica Acta, 2006. **52**(1): p. 221-233.
8. Shao, M.H. and R.R. Adzic, *Electrooxidation of ethanol on a Pt electrode in acid solutions: in situ ATR-SEIRAS study.* Electrochimica Acta, 2005. **50**(12): p. 2415-2422.
9. Del Colle, V., J. Souza-Garcia, G. Tremiliosi-Filho, E. Herrero, and J.M. Feliu, *Electrochemical and spectroscopic studies of ethanol oxidation on Pt stepped surfaces modified by tin adatoms.* Phys Chem Chem Phys, 2011. **13**(26): p. 12163-72.
10. Jiang, L., L. Colmenares, Z. Jusys, G.Q. Sun, and R.J. Behm, *Ethanol electrooxidation on novel carbon supported Pt/SnOx/C catalysts with varied Pt : Sn ratio.* Electrochimica Acta, 2007. **53**(2): p. 377-389.
11. Zhou, W.P., S. Axnanda, M.G. White, R.R. Adzic, and J. Hrbek, *Enhancement in Ethanol Electrooxidation by SnOx Nanoislands Grown on Pt(111): Effect of Metal Oxide-Metal Interface Sites.* Journal of Physical Chemistry C, 2011. **115**(33): p. 16467-16473.
12. Zhou, W.P., W. An, D. Su, R. Palomino, P. Liu, M.G. White, and R.R. Adzic, *Electrooxidation of Methanol at SnOx-Pt Interface: A Tunable Activity of Tin Oxide Nanoparticles.* Journal of Physical Chemistry Letters, 2012. **3**(22): p. 3286-3290.
13. Chinchen, G.C., P.J. Denny, J.R. Jennings, M.S. Spencer, and K.C. Waugh, *Synthesis of Methanol.* Applied Catalysis, 1988. **36**: p. 1-65.
14. Burch, R. and M.I. Petch, *Investigation of the Synthesis of Oxygenates from Carbon-Monoxide Hydrogen Mixtures on Supported Rhodium Catalysts.* Applied Catalysis A: General, 1992. **88**(1): p. 39-60.
15. Haider, M.A., M.R. Gogate, and R.J. Davis, *Fe-promotion of supported Rh catalysts for direct conversion of syngas to ethanol.* Journal of Catalysis, 2009. **261**(1): p. 9-16.
16. Spivey, J.J. and A. Egbebi, *Heterogeneous catalytic synthesis of ethanol from biomass-derived syngas.* Chem Soc Rev, 2007. **36**(9): p. 1514-28.

17. Lamy, C., E.M. Belgsir, and J.M. Léger, *Electrocatalytic oxidation of aliphatic alcohols: Application to the direct alcohol fuel cell (DAFC).* Journal of Applied Electrochemistry, 2001. **31**(7): p. 799-809.
18. Kutz, R.B., B. Braunschweig, P. Mukherjee, R.L. Behrens, D.D. Dlott, and A. Wieckowski, *Reaction pathways of ethanol electrooxidation on polycrystalline platinum catalysts in acidic electrolytes.* Journal of Catalysis, 2011. **278**(2): p. 181-188.
19. Koper, M.T.M., S.C.S. Lai, and E. Herrero, *Electrocatalysis for the Direct Alcohol Fuel Cell*, in *Fuel cell catalysis: a surface science approach*, M.T.M. Koper, Editor. 2009, John Wiley & Sons, Inc.: Hoboken, New Jersy.
20. Colmati, F., G. Tremiliosi-Filho, E.R. Gonzalez, A. Berna, E. Herrero, and J.M. Feliu, *The role of the steps in the cleavage of the C-C bond during ethanol oxidation on platinum electrodes.* Phys Chem Chem Phys, 2009. **11**(40): p. 9114-23.
21. Chang, S.C., L.W.H. Leung, and M.J. Weaver, *Metal Crystallinity Effects in Electrocatalysis as Probed by Real-Time Ftir Spectroscopy - Electrooxidation of Formic-Acid, Methanol, and Ethanol on Ordered Low-Index Platinum Surfaces.* Journal of Physical Chemistry, 1990. **94**(15): p. 6013-6021.
22. Tarnowski, D.J. and C. Korzeniewski, *Effects of surface step density on the electrochemical oxidation of ethanol to acetic acid.* Journal of Physical Chemistry B, 1997. **101**(2): p. 253-258.
23. Iwasita, T. and E. Pastor, *A DEMS and FTIR Spectroscopic Investigation of Adsorbed Ethanol on Polycrystalline Platinum.* Electrochimica Acta, 1994. **39**(4): p. 531-537.
24. Heinen, M., Z. Jusys, and R.J. Behm, *Ethanol, Acetaldehyde and Acetic Acid Adsorption/Electrooxidation on a Pt Thin Film Electrode under Continuous Electrolyte Flow: An in Situ ATR-FTIRS Flow Cell Study.* Journal of Physical Chemistry C, 2010. **114**(21): p. 9850-9864.
25. Jiang, L., G. Sun, Z. Zhou, S. Sun, Q. Wang, S. Yan, H. Li, J. Tian, J. Guo, B. Zhou, and Q. Xin, *Size-controllable synthesis of monodispersed SnO2 nanoparticles and application in electrocatalysts.* J Phys Chem B, 2005. **109**(18): p. 8774-8.
26. Mann, J., N. Yao, and A.B. Bocarsly, *Characterization and analysis of new catalysts for a direct ethanol fuel cell.* Langmuir, 2006. **22**(25): p. 10432-6.
27. Silva, J.C.M., L.S. Parreira, R.F.B. De Souza, M.L. Calegaro, E.V. Spinace, A.O. Neto, and M.C. Santos, *PtSn/C alloyed and non-alloyed materials: Differences in the ethanol electro-oxidation reaction pathways.* Applied Catalysis B-Environmental, 2011. **110**: p. 141-147.
28. Alcala, R., J.W. Shabaker, G.W. Huber, M.A. Sanchez-Castillo, and J.A. Dumesic, *Experimental and DFT studies of the conversion of ethanol and acetic acid on PtSn-based catalysts.* J Phys Chem B, 2005. **109**(6): p. 2074-85.
29. Scott, F.J., S. Mukerjee, and D.E. Ramaker, *Contrast in Metal-Ligand Effects on PtnM Electrocatalysts with M Equal Ru vs Mo and Sn As Exhibited by in Situ XANES and EXAFS Measurements in Methanol.* Journal of Physical Chemistry C, 2010. **114**(1): p. 442-453.
30. Zhu, M.Y., G.Q. Sun, and Q. Xin, *Effect of alloying degree in PtSn catalyst on the catalytic behavior for ethanol electro-oxidation.* Electrochimica Acta, 2009. **54**(5): p. 1511-1518.

31. Seidel, Y.E., A. Schneider, Z. Jusys, B. Wickman, B. Kasemo, and R.J. Behm, *Mesoscopic mass transport effects in electrocatalytic processes.* Faraday Discussions, 2009. **140**(0): p. 167-184.
32. Del Colle, V., A. Berna, G. Tremiliosi-Filho, E. Herrero, and J.M. Feliu, *Ethanol electrooxidation onto stepped surfaces modified by Ru deposition: electrochemical and spectroscopic studies.* Phys Chem Chem Phys, 2008. **10**(25): p. 3766-73.
33. Kutz, R.B., B. Braunschweig, P. Mukherjee, D.D. Dlott, and A. Wieckowski, *Study of Ethanol Electrooxidation in Alkaline Electrolytes with Isotope Labels and Sum-Frequency Generation.* Journal of Physical Chemistry Letters, 2011. **2**(17): p. 2236-2240.
34. Yang, L. and P. Liu, *Ethanol Synthesis from Syngas on Transition Metal-Doped Rh(111) Surfaces: A Density Functional Kinetic Monte Carlo Study.* Topics in Catalysis, 2014. **57**(1-4): p. 125-134.
35. Liu, Y., K. Murata, M. Inaba, I. Takahara, and K. Okabe, *Synthesis of ethanol from syngas over $Rh/Ce_{1-x}Zr_xO_2$ catalysts.* Catalysis Today, 2011. **164**(1): p. 308-314.
36. Gao, J., X.H. Mo, and J.G. Goodwin, *La, V, and Fe promotion of Rh/SiO_2 for CO hydrogenation: Detailed analysis of kinetics and mechanism.* Journal of Catalysis, 2009. **268**(1): p. 142-149.
37. Choi, Y. and P. Liu, *Mechanism of ethanol synthesis from syngas on Rh(111).* Journal of the American Chemical Society, 2009. **131**(36): p. 13054-61.
38. Subramani, V. and S.K. Gangwal, *A review of recent literature to search for an efficient catalytic process for the conversion of syngas to ethanol.* Energy & Fuels, 2008. **22**(2): p. 814-839.
39. Chuang, S.S.C., R.W. Stevens, and R. Khatri, *Mechanism of C_{2+} oxygenate synthesis on Rh catalysts.* Topics in Catalysis, 2005. **32**(3-4): p. 225-232.
40. Burch, R. and M.J. Hayes, *The preparation and characterisation of Fe-promoted Al_2O_3-supported Rh catalysts for the selective production of ethanol from syngas.* Journal of Catalysis, 1997. **165**(2): p. 249-261.
41. Orita, H., S. Naito, and K. Tamaru, *Mechanism of Acetaldehyde Formation from the Carbon-Monoxide Hydrogen Reaction Below Atmospheric-Pressure over Supported Rh Catalysts.* Journal of the Chemical Society-Chemical Communications, 1984(3): p. 150-151.
42. Egbebi, A., V. Schwartz, S.H. Overbury, and J.J. Spivey, *Effect of Li Promoter on titania-supported Rh catalyst for ethanol formation from CO hydrogenation.* Catalysis Today, 2010. **149**(1-2): p. 91-97.
43. Mo, X.H., J. Gao, and J.G. Goodwin, *Role of promoters on Rh/SiO_2 in CO hydrogenation: A comparison using DRIFTS.* Catalysis Today, 2009. **147**(2): p. 139-149.
44. Mo, X.H., J. Gao, N. Umnajkaseam, and J.G. Goodwin, *La, V, and Fe promotion of Rh/SiO_2 for CO hydrogenation: Effect on adsorption and reaction.* Journal of Catalysis, 2009. **267**(2): p. 167-176.
45. Madier, Y., C. Descorme, A.M. Le Govic, and D. Duprez, *Oxygen Mobility in CeO_2 and $Ce_xZr_{(1-x)}O_2$ Compounds: Study by CO Transient Oxidation and $^{18}O/^{16}O$ Isotopic Exchange.* Journal of Physical Chemistry B, 1999. **103**(50): p. 10999-11006.
46. Bunluesin, T., R.J. Gorte, and G.W. Graham, *Studies of the water-gas-shift reaction on ceria-supported Pt, Pd, and Rh: implications for oxygen-storage properties.* Applied Catalysis B: Environmental, 1998. **15**(1-2): p. 107-114.

47. Fu, Q., A. Weber, and M. Flytzani-Stephanopoulos, *Nanostructured Au-CeO_2 catalysts for low-temperature water-gas shift.* Catalysis Letters, 2001. **77**(1-3): p. 87-95.
48. Li, C.M., J.M. Liu, W. Gao, Y.F. Zhao, and M. Wei, *Ce-Promoted Rh/TiO_2 Heterogeneous Catalysts Towards Ethanol Production from Syngas.* Catalysis Letters, 2013. **143**(11): p. 1247-1254.
49. Basu, P., T.H. Ballinger, and J.T. Yates, *Wide Temperature-Range Ir Spectroscopy Cell for Studies of Adsorption and Desorption on High Area Solids.* Review of Scientific Instruments, 1988. **59**(8): p. 1321-1327.
50. Yates, J.T., T.M. Duncan, and R.W. Vaughan, *Infrared Spectroscopic Study of Activated Surface Processes - Co-Chemisorption on Supported Rh.* Journal of Chemical Physics, 1979. **71**(10): p. 3908-3915.
51. Yates, J.T., T.M. Duncan, S.D. Worley, and R.W. Vaughan, *Infrared-Spectra of Chemisorbed Co on Rh.* Journal of Chemical Physics, 1979. **70**(3): p. 1219-1224.
52. Yang, A.C. and C.W. Garland, *Infrared Studies of Carbon Monoxide Chemisorbed on Rhodium.* Journal of Physical Chemistry, 1957. **61**(11): p. 1504-1512.
53. Basu, P., D. Panayotov, and J.T. Yates, *Rhodium-carbon monoxide surface chemistry: the involvement of surface hydroxyl groups on alumina and silica supports.* Journal of the American Chemical Society, 1988. **110**(7): p. 2074-2081.
54. Trautmann, S. and M. Baerns, *Infrared Spectroscopic Studies of CO Adsorption on Rhodium Supported by SiO_2, Al_2O_3, and TiO_2.* Journal of Catalysis, 1994. **150**(2): p. 335-344.
55. Kraus, L., M.I. Zaki, H. Knozinger, and B. Tesche, *Support and Additive Effects on the State of Rhodium Catalysts.* Journal of Molecular Catalysis, 1989. **55**(1-3): p. 55-69.
56. Panayotov, D., M. Mihaylov, D. Nihtianova, T. Spassov, and K. Hadjiivanov, *Spectral evidence for hydrogen-induced reversible segregation of CO adsorbed on titania-supported rhodium.* Physical Chemistry Chemical Physics, 2014. **16**(26): p. 13136-44.
57. Couble, J. and D. Bianchi, *Heats of adsorption of linear CO species adsorbed on reduced Fe/Al_2O_3 catalysts using the AEIR method in diffuse reflectance mode.* Applied Catalysis A: General, 2011. **409**: p. 28-38.
58. Wielers, A.F.H., A.J.H.M. Kock, C.E.C.A. Hop, J.W. Geus, and A.M. van Der Kraan, *The reduction behavior of silica-supported and alumina-supported iron catalysts: A Mössbauer and infrared spectroscopic study.* Journal of Catalysis, 1989. **117**(1): p. 1-18.
59. Johnston, C., N. Jorgensen, and C.H. Rochester, *Volumetric and Infrared Studies of Carbon-Monoxide Adsorption on Silica-Supported Iron Catalysts Characterized by Thermogravimetric Analysis and X-Ray-Diffraction.* Journal of the Chemical Society, Faraday Transactions 1: Physical Chemistry in Condensed Phases, 1988. **84**(1): p. 309-319.
60. Chudek, J.A., M.W. McQuire, G.W. McQuire, and C.H. Rochester, *In situ FTIR study of CO–H_2 reactions over Rh/TiO_2 catalysts at high pressure and temperature.* J. Chem. Soc., Faraday Trans., 1994. **90**(24): p. 3699-3709.
61. Mcquire, M.W., C.H. Rochester, and J.A. Anderson, *Syngas Reactions over Rh/SiO_2 at High-Pressure and Temperature Studied by Fourier-Transform Infrared-Spectroscopy.* Journal of the Chemical Society, Faraday Transactions, 1992. **88**(6): p. 879-886.
62. Prieto, G., P. Concepcion, A. Martinez, and E. Mendoza, *New insights into the role of the electronic properties of oxide promoters in Rh-catalyzed selective synthesis of oxygenates from synthesis gas.* Journal of Catalysis, 2011. **280**(2): p. 274-288.

63. Fukushima, T., H. Arakawa, and M. Ichikawa, *High-pressure IR spectroscopic evidence of acetyl and acetate species directly formed in CO–H_2 conversion on SiO_2-supported Rh and Rh–Mn catalysts.* J. Chem. Soc., Chem. Commun., 1985(11): p. 729-731.
64. Fukushima, T., H. Arakawa, and M. Ichikawa, *In situ high-pressure FT-IR studies on the surface species formed in carbon monoxide hydrogenation on silicon dioxide-supported rhodium-iron catalysts.* Journal of Physical Chemistry, 1985. **89**(21): p. 4440-4443.
65. Underwood, R.P. and A.T. Bell, *Lanthana-promoted Rh/SiO_2: II. Studies of CO hydrogenation.* Journal of Catalysis, 1988. **111**(2): p. 325-335.
66. Trevino, H., T. Hyeon, and W.M.H. Sachtler, *A novel concept for the mechanism of higher oxygenate formation from synthesis gas over MnO-promoted rhodium catalysts.* Journal of Catalysis, 1997. **170**(2): p. 236-243.
67. Lochar, V., *FT-IR study of methanol, formaldehyde and methyl formate adsorption on the surface of Mo/Sn oxide catalyst.* Applied Catalysis A: General, 2006. **309**(1): p. 33-36.
68. Wu, W.C., C.C. Chuang, and J.L. Lin, *Bonding geometry and reactivity of methoxy and ethoxy groups adsorbed on powdered TiO_2.* Journal of Physical Chemistry B, 2000. **104**(36): p. 8719-8724.
69. Yu, Z.Q. and S.S.C. Chuang, *In situ IR study of adsorbed species and photogenerated electrons during photocatalytic oxidation of ethanol on TiO2.* Journal of Catalysis, 2007. **246**(1): p. 118-126.
70. Trevino, H., G.D. Lei, and W.M.H. Sachtler, *Co Hydrogenation to Higher Oxygenates over Promoted Rhodium - Nature of the Metal-Promoter Interaction in Rhmn/Nay.* Journal of Catalysis, 1995. **154**(2): p. 245-252.
71. Falk, M. and E. Whalley, *Infrared Spectra of Methanol and Deuterated Methanols in Gas, Liquid, and Solid Phases.* Journal of Chemical Physics, 1961. **34**(5): p. 1554-1568.
72. Takeuchi, A. and J.R. Katzer, *Mechanism of Methanol Formation.* Journal of Physical Chemistry, 1981. **85**(8): p. 937-939.
73. Xu, W.Q., Z.Y. Liu, A.C. Johnston-Peck, S.D. Senanayake, G. Zhou, D. Stacchiola, E.A. Stach, and J.A. Rodriguez, *Steam Reforming of Ethanol on Ni/CeO_2: Reaction Pathway and Interaction between Ni and the CeO_2 Support.* ACS Catalysis, 2013. **3**(5): p. 975-984.
74. Li, C., Y. Sakata, T. Arai, K. Domen, K.-i. Maruya, and T. Onishi, *Adsorption of carbon monoxide and carbon dioxide on cerium oxide studied by Fourier-transform infrared spectroscopy. Part 2.—Formation of formate species on partially reduced CeO_2 at room temperature.* Journal of the Chemical Society, Faraday Transactions 1: Physical Chemistry in Condensed Phases, 1989. **85**(6): p. 1451.
75. Li, D., S. Sakai, Y. Nakagawa, and K. Tomishige, *FTIR study of CO adsorption on Rh/MgO modified with Co, Ni, Fe, or CeO_2 for the catalytic partial oxidation of methane.* Physical Chemistry Chemical Physics, 2012. **14**(25): p. 9204-13.
76. Hoffmann, M.R., S.T. Martin, W. Choi, and D.W. Bahnemann, *Environmental Applications of Semiconductor Photocatalysis.* Chemical Reviews, 1995. **95**(1): p. 69-96.
77. Linsebigler, A.L., G. Lu, and J.T. Yates, *Photocatalysis on TiO_2 Surfaces: Principles, Mechanisms, and Selected Results.* Chemical Reviews, 1995. **95**(3): p. 735-758.
78. Schneider, J., M. Matsuoka, M. Takeuchi, J. Zhang, Y. Horiuchi, M. Anpo, and D.W. Bahnemann, *Understanding TiO_2 Photocatalysis: Mechanisms and Materials.* Chemical Reviews, 2014. **114**(19): p. 9919-9986.

79. Fujishima, A., X. Zhang, and D.A. Tryk, *TiO_2 photocatalysis and related surface phenomena.* Surface Science Reports, 2008. **63**(12): p. 515-582.
80. Henderson, M.A., W.S. Epling, C.H.F. Peden, and C.L. Perkins, *Insights into Photoexcited Electron Scavenging Processes on TiO_2 Obtained from Studies of the Reaction of O_2 with OH Groups Adsorbed at Electronic Defects on TiO_2(110).* The Journal of Physical Chemistry B, 2003. **107**(2): p. 534-545.
81. Zehr, R.T. and M.A. Henderson, *Acetaldehyde photochemistry on TiO_2(1 1 0).* Surface Science, 2008. **602**(13): p. 2238-2249.
82. Coronado, J.M., S. Kataoka, I. Tejedor-Tejedor, and M.A. Anderson, *Dynamic phenomena during the photocatalytic oxidation of ethanol and acetone over nanocrystalline TiO_2: simultaneous FTIR analysis of gas and surface species.* Journal of Catalysis, 2003. **219**(1): p. 219-230.
83. Henderson, M.A., *Photooxidation of Acetone on TiO_2(110): Conversion to Acetate via Methyl Radical Ejection.* The Journal of Physical Chemistry B, 2005. **109**(24): p. 12062-12070.
84. Ohsawa, T., I.V. Lyubinetsky, M.A. Henderson, and S.A. Chambers, *Hole-Mediated Photodecomposition of Trimethyl Acetate on a TiO_2(001) Anatase Epitaxial Thin Film Surface.* The Journal of Physical Chemistry C, 2008. **112**(50): p. 20050-20056.
85. Savory, D.M., D.S. Warren, and A.J. McQuillan, *Shallow Electron Trap, Interfacial Water, and Outer-Sphere Adsorbed Oxalate IR Absorptions Correlate during UV Irradiation of Photocatalytic TiO_2 Films in Aqueous Solution.* The Journal of Physical Chemistry C, 2011. **115**(4): p. 902-907.
86. Connor, P.A., K.D. Dobson, and A.J. McQuillan, *Infrared Spectroscopy of the TiO_2/Aqueous Solution Interface.* Langmuir, 1999. **15**(7): p. 2402-2408.
87. Warren, D.S. and A.J. McQuillan, *Influence of Adsorbed Water on Phonon and UV-Induced IR Absorptions of TiO_2 Photocatalytic Particle Films.* The Journal of Physical Chemistry B, 2004. **108**(50): p. 19373-19379.
88. Yoshihara, T., R. Katoh, A. Furube, Y. Tamaki, M. Murai, K. Hara, S. Murata, H. Arakawa, and M. Tachiya, *Identification of Reactive Species in Photoexcited Nanocrystalline TiO_2 Films by Wide-Wavelength-Range (400−2500 nm) Transient Absorption Spectroscopy.* The Journal of Physical Chemistry B, 2004. **108**(12): p. 3817-3823.
89. Topalian, Z., B.I. Stefanov, C.G. Granqvist, and L. Österlund, *Adsorption and photo-oxidation of acetaldehyde on TiO_2 and sulfate-modified TiO_2: Studies by in situ FTIR spectroscopy and micro-kinetic modeling.* Journal of Catalysis, 2013. **307**: p. 265-274.
90. Raskó, J. and J. Kiss, *Adsorption and surface reactions of acetaldehyde on TiO_2, CeO_2 and Al_2O_3.* Applied Catalysis A: General, 2005. **287**(2): p. 252-260.
91. Singh, M., N. Zhou, D.K. Paul, and K.J. Klabunde, *IR spectral evidence of aldol condensation: Acetaldehyde adsorption over TiO_2 surface.* Journal of Catalysis, 2008. **260**(2): p. 371-379.
92. McEntee, M., A. Stevanovic, W. Tang, M. Neurock, and J.T. Yates, *Electric Field Changes on Au Nanoparticles on Semiconductor Supports – The Molecular Voltmeter and Other Methods to Observe Adsorbate-Induced Charge-Transfer Effects in Au/TiO_2 Nanocatalysts.* Journal of the American Chemical Society, 2015. **137**(5): p. 1972-1982.